2017

Simulation of Diesel Particulate Filter regeneration using Lattice Boltzmann method

Kshitiz Kumar Jain
Michigan Technological University, kkjain@mtu.edu

SIMULATION OF DIESEL PARTICULATE FILTER REGENERATION USING LATTICE BOLTZMANN METHOD

By

Kshitiz Kumar Jain

A REPORT

Submitted in partial fulfillment of the requirements for the degree of

MASTER OF SCIENCE

In Mechanical Engineering

MICHIGAN TECHNOLOGICAL UNIVERSITY

2017

This report has been approved in partial fulfillment of the requirements for the Degree of MASTER OF SCIENCE in Mechanical Engineering.

Department of Mechanical Engineering-Engineering Mechanics

Report Advisor:	*Dr. Song-Lin Yang*
Committee Member:	*Dr. Kazuya Tajiri*
Committee Member:	*Dr. Sajjad Bigham*
Department Chair:	*Dr. William W. Predebon*

Dedication

To my parents, Vinita and Sudhir

The two pillars of my life.

Table of Contents

List of Figures

Acknowledgements

The process of earning a master's degree and writing this report has been a long and arduous one, and it certainly was not accomplished single-handedly. First, and foremost, I would like to thank Dr. Song-Lin (Jason) Yang, professor, mentor and research advisor extraordinaire. Without his help, advice and expertise, this research and report would not have happened.

Dr. Kazuya Tajiri and Dr. Sajjad Bigham, provided me with insight and invaluable feedback as my committee members which is greatly appreciated.

I am grateful to my parents, Sudhir and Vinita Jain, for their constant love and support through the past twenty-four odd years. My brother Arth, who has been a constant source of joy in my life.

I would certainly be remiss not to mention and thank Aamir Ibrahim for all his help, not just as a colleague but also as a friend.

Lastly, I want to thank all my friends at Michigan Tech and back home for their support.

Abstract

Lattice Boltzmann Method is a novel approach, which has shown promise in solving a wide variety of fluid flow problems including single and multi-phase flows in complex geometries. Volume elements of the fluid domain are considered to be composed of particles and these particles fall under a velocity distribution function at each grid point. Particles collide with each other under the influence of external forces and the rules of collision are defined so as to be compatible with the Navier-Stokes Equation. In the current work, LBM has been applied to Diesel Particulate filters which is a device used for reducing Particulate Matter emissions from diesel engines. Diesel Particulate Filtering (DPF) technologies as they are collectively known, have a two-step mechanism to them. First is the trapping of the particulate matter and second is the regeneration process, which is essentially the cleaning process applied to get rid of the trapped soot with or without the help of catalytic compounds. The deposited soot is oxidized during this regeneration process. This oxidation of soot has been modeled in the current work using LBM. An artificially created porous microstructure as used by authors in some earlier works has been used to simulate the flow of fluid, which is considered to have a specified mass fraction of soot for different runs of the simulation. The velocity and concentration fields have been modeled with a D2Q9 lattice arrangement and the temperature field with a D2Q4 arrangement. The numerical code is developed using C. Flow over a heated cylinder has been modeled as a benchmark case. The pressure, velocity, temperature and concentration contours for the disordered media are compared with published work.

1 Introduction

Vehicles have played a key role in the development of society. But, like many other human inventions, vehicles come with a major drawback – pollution. Burning fuel in a combustion engine emits pollutants which has hazardous impacts on human health and environment. Particulate matter (PM) is one such pollutant which has carcinogenic effects on human body and constitutes as the major reason for visibility impairment in the normal atmosphere. The definition of Particulate matter is ambiguous because PM comes in different shapes, sizes, chemical structures and particle mass. Diesel particulate filters (DPFs) are a type of device developed for controlling PM. The increasingly stringent regulations due to the adverse effects of PM and other such pollutants on human health and environment makes it very important to study after-treatment devices like Diesel Particulate filters.

As the name suggests, DPFs are a type of filter designed to tap the PM inside before releasing the exhaust into the atmosphere. They have a porous structure to allow the exhaust to pass through but the soot (PM) is trapped. This accumulates the soot inside the filter. Hence, it is of utmost importance to take care of the change in flow field inside the filter as soot accumulates and blocks the passage of the exhaust gases. This blockage increases the back-pressure which causes the problem of increased fuel consumption. If the accumulated soot is not cleaned, eventually engine operation would be hindered. This is where the term ‘regeneration’ is introduced. DPF regeneration is basically the clean-up process applied at regular intervals to get rid of the accumulated soot through combustion.

In recent times, pore scale simulations of the flow in diesel particulate filters is gaining popularity due to the difficulty faced by the numerous experimental studies of DPFs in observing them. It is even more difficult to observe the regeneration process due to a comparatively smaller extent of the exact reaction mechanisms involved in the process and the high reaction rates during the combustion. The present study aims at simulating the regeneration phenomena in a diesel particulate filter. Lattice Boltzmann method has

been applied for the simulation due to its superiority in applying boundary conditions to complex geometries such as that of porous media in a filter. Also, LBM has shown great suitability to flow through porous media. There have been many studies conducted on the simulation of porous media flow using LBM most of which make use of tomographic scans of the insides of a DPF. The current study uses of a computer generated porous media as opposed to the tomography assisted one mentioned above. Another major difference between this study and the ones mentioned above is that this study makes use of an incompressible approach to LBM which is capable of generating results which are more realistic than the other studies. The reason behind that claim is that all other studies make use of a more pseudo-incompressible approach to LBM but most pore scale flows are incompressible in nature.

1.1 Objectives

There are two major objectives of this study as mentioned in the following subsections.

1.1.1 Simulating Regeneration phenomenon in diesel particulate filters

In the current work, regeneration phenomenon in particulate filters is simulated by making use of the virtual substrate generator and the incompressible Lattice Boltzmann method. An original computational model based on pressure drop calculation and temperature fluctuations has been developed for the simulation of regeneration process. The chemistry of the soot oxidation has been incorporated with detail into the model. The results obtained using the model are compared against experimental data from literature for validation. Also, basic physical considerations like the conservation equations have been employed to test the validity.

1.1.2 Validating the i-LBM for flow through diesel particulate filters

The simulation in this study takes into consideration three major phenomena going inside the filter. Transport, deposition or soot accumulation, and regeneration and the temperature variation that accompanies it, in that order. The entire simulation makes use of the incompressible LBM described above. The i-LBM has been validated for the

transport and deposition phenomena in an earlier work [1]. This report focuses on the validity of the i-LBM for the simulation of the temperature field through the DPF which is the controlling factor of the regeneration process.

1.2 Outline

This report consists of an introduction and 5 chapters. Chapter 2 discusses the background and the formulation of the Lattice Boltzmann method in detail. Also included in this chapter is an introduction to the incompressible LBM and a brief idea of its formulation. Additionally, this chapter holds a concise description of the boundary conditions and their implementation.

Chapter 3 presents a look in to the diesel particulate filters and their inner workings. The varied materials that go into the making of a DPF, inner structure, pathway of the flow and the mechanism of the soot accumulation are described in detail in this chapter. Most importantly, the phenomenon of regeneration and the several ways of its application are presented and classified in this chapter.

Chapter 4 provides an understanding of the actual numerical simulation of the phenomenon. A little background into the previous work on porous media generation and the simulation of the transport and deposition phenomenon is presented for better understanding of the current simulation. The computational model for regeneration is explained in detail in this chapter.

Chapter 5 summarizes the results of the study and the inferences drawn from those results. For better understanding and further validity, a parametric study was performed, the results of which have been presented.

Conclusions drawn on the entire study and some recommendations for future work make the contents of chapter 6.

2 Lattice Boltzmann Method

This section presents a review of the Lattice Boltzmann Method (LBM), a relatively novel approach of solving fluid flow problems. LBM has shown great promise in solving problems with complex boundary conditions, multiphase flows and more recently, fluid turbulence and reaction diffusion systems. LBM develops simplistic kinetic equation by making use of the mesoscopic processes in a way that allows for the macroscopic averaged properties to follow the desired equations. This contrasts with the macroscopic approach of the other, more conventional numerical schemes. The idea is to model the microscopic physics in a way such that the averaged properties follow the macroscopic equations. The macroscopic flow is unaffected by the intricate details of the microscopic physics because of it being the result of the collective averaged behavior of the microscopic particles [2]. This simplification of the kinetic equation allows for the elimination of the need to solve the complicated kinetic equations like the full Boltzmann equation, as well as it eliminates the need to follow the trajectory of each individual particle [3].

Since LBM is mesoscopic in nature, unlike the other numerical schemes that use macroscopic formulation, its streaming process (or the convection operator) is linear in phase (or velocity) space as opposed to the non-linear streaming process in the macroscopic numerical schemes [3]. Second major difference between LBM and the other conventional schemes, is its nearly incompressible limit that allows the incompressible Navier-Stokes equation to be obtained by calculating the pressure using an equation of state. Other conventional schemes solve the incompressible Navier-Stokes equation along with the Poisson equation with velocity strains as sources. This complicates the calculations and numerous assumptions must be made. Thirdly, there are only a limited number of velocities to be considered in the phase space of LBM, as opposed to the complete functionality of velocity phase space in the kinetic theory. One or two velocities with a handful of moving directions makes the transformation of macroscopic quantities from mesoscopic distribution functions simpler and easy to calculate.

2.1 Lattice gas automata

The origin of LBM is often traced back to the 1970s, from the lattice gas (LG) automata [4, 5]. A lattice gas automaton is a molecular dynamic which is imaginary and where the space, time, and particle velocities are all discrete, essentially defining a 'cell'. Thereby, the name lattice gas cellular automata. This 'cell' or 'lattice' has particles residing on its nodes and each particle has its own set of Boolean variables $n_i(\mathbf{x},t)(i=1,...,M)$ describing the particle's occupation. '*M'* is the number of directions of particle velocities at each node. The evolution equation of LG automata involves two steps, namely, streaming and collision. Each particle moves to the next node according to the streaming step in the direction of its velocity, where it interacts with another particle according to the collision rule.

The Lattice Boltzmann Method replaces the Boolean variables with single particle distribution functions and ignores the individual particle-particle interaction in the kinetic equations [6].

2.2 Lattice Boltzmann equations: LG automata extended

The Lattice Boltzmann Method replaces the Boolean variables, n_i (particle occupation variables), with single particle distribution functions, $f_i = \langle n_i \rangle$, and ignores the individual particle motion in the kinetic equations. Here, $\langle . \rangle$ denotes the ensemble average. These averaged particle distributions are the original variables in LBM, which are mesoscopic in nature. However, the kinetic form is still the same as the LG automata and hence, the advantages of locality in the kinetic form are preserved [3].

The evolution equation of lattice gas automata is given as:

$$n_i(\mathbf{x}+\mathbf{e}_i, t+1) = n_i(\mathbf{x},t) + \Omega_i(n(\mathbf{x},t)) \qquad (i=0,1,...,M), \qquad (1)$$

where, $\mathbf{e}_i$ are the local particle velocities.

This equation is modified by replacing the Boolean variables, n_i, with the distribution functions, $f_i = \langle n_i \rangle$, as follows:

$$f_i(\mathbf{x} + \mathbf{e}_i \Delta t, t + \Delta t) = f_i(\mathbf{x}, t) + \Omega_i(f(\mathbf{x}, t)), \qquad (i = 0, 1, ..., M), \qquad (2)$$

where f_i is the particle velocity distribution function along the i^{th} direction, $\Omega_i = \Omega_i(f(\mathbf{x}, t))$ is the collision operator. Ω_i is the rate of change of f_i resulting from collision and depends only on the local distribution function. Δt and Δx are steps in time and space. If $\Delta x / \Delta t = |\mathbf{e}_i|$, the discretization of equations (1) and (2) would be the same - $\mathbf{x} + \mathbf{e}_i$ would be the coordinates for the nearest points around $\mathbf{x}$.

The density ρ and the momentum density $\rho\mathbf{u}$ can be written as the particle velocity moments of the distribution function, f_i:

$$\rho = \sum_{i=1}^{M} f_i \qquad \text{and} \qquad \rho\mathbf{u} = \sum_{i=1}^{M} f_i \mathbf{e}_i \qquad (3)$$

Now, Ω_i needs to satisfy the conservation of mass and momentum, implying:

$$\sum_i \Omega_i = 0 \qquad \text{and} \qquad \sum_i \Omega_i \mathbf{e}_i = 0 \qquad (4)$$

The space and time increments, Δx and Δt, can be small parameters of the same order, say $\boldsymbol{\varepsilon}$, for long wavelength and low frequency domain. Applying Taylor series expansion in time and space, a kinetic equation is obtained:

$$\frac{\partial f_i}{\partial t} + \mathbf{e}_i \cdot \frac{\partial}{\partial x_i} f_i + \varepsilon \left(\frac{1}{2} \mathbf{e}_i \mathbf{e}_i : \frac{\partial^2}{\partial x_i^2} f_i + \mathbf{e}_i \cdot \frac{\partial}{\partial x_i} \frac{\partial f_i}{\partial t} + \frac{1}{2} \frac{\partial^2 f_i}{\partial t^2} \right) = \frac{\Omega_i}{\varepsilon} \qquad (5)$$

At this point, the need arises to develop a relationship between LBM and macro-scale system. The Chapman-Enskog expansion is employed to derive the macroscopic hydrodynamic equation [7],

$$\frac{\partial}{\partial t} = \varepsilon \frac{\partial}{\partial t_1} + \varepsilon^2 \frac{\partial}{\partial t_2}, \qquad \frac{\partial}{\partial x} = \varepsilon \frac{\partial}{\partial x_1}$$

Here, t_1 is the convection time scale and t_2 is the diffusion time scale. And it is assumed that $t_2 << t_1$.

Similarly, the one particle distribution function can be rewritten as:

$$f_i = f_i^{eq} + \varepsilon f_i^{(neq)} \tag{6}$$

Here, f_i^{eq} is the local equilibrium distribution function and depends on the macroscopic variables (ρ and $\rho\mathbf{u}$). Hence,

$$\sum_i f_i^{eq} = \rho, \qquad \sum_i f_i^{eq}\mathbf{e}_i = \rho\mathbf{u} \tag{7}$$

and, $f_i^{(neq)} = f_i^{(1)} + \varepsilon f_i^{(2)} + O(\varepsilon^2)$ is the non-equilibrium distribution function. It has the following limitations:

$$\sum_i f_i^{(k)} = 0 \quad \text{and} \quad \sum_i f_i^{(k)}\mathbf{e}_i = 0 \qquad \text{for k=1, 2} \tag{8}$$

Writing the collision operator with f_i, the Taylor expansion gives:

$$\Omega_i(f) = \Omega_i(f^{eq}) + \in \frac{\partial \Omega_i(f^{eq})}{\partial f_i} f_j^{(1)} + \in^2 \left(\frac{\partial \Omega_i(f^{eq})}{\partial f_j} f_j^{(2)} + \frac{\partial^2 \Omega_i(f^{eq})}{\partial f_j \partial f_k} f_j^{(1)} f_k^{(1)} \right) + O(\varepsilon^3) \tag{9}$$

If $\varepsilon \to 0$, then $\Omega_i(f^{eq}) = 0$, which gives:

$$\frac{\Omega_i(f)}{\varepsilon} = \frac{M_{ij}}{\varepsilon}(f_j + f_j^{eq}), \tag{10}$$

where $M_{ij} \equiv \frac{\partial \Omega_i(f^{eq})}{\partial f_j}$ is the collision matrix [8], which determines the scattering rate between directions *i* and *j*. M_{ij} has a limited set of values and it only depends on the angle between the two directions. M_{ij} must satisfy the following constraints:

$$\sum_{i=1}^{M} M_{ij} = 0 \qquad \text{and} \qquad \sum_{i=1}^{M} \mathbf{e}_i M_{ij} = 0 \tag{11}$$

In addition, if we assume that the equilibrium state is achieved by the local particle distribution at a constant relaxation rate of τ ,

$$M_{ij} = -\frac{1}{\tau}\delta_{ij} \tag{12}$$

And thus, we arrive at the Lattice Bhatnagar-Gross-Krook (LBGK) collision operator [9],

$$\frac{\Omega_i}{\varepsilon} = -\frac{1}{\tau} f_i^{(neq)} = -\frac{1}{\varepsilon\tau}(f_i^{(1)} + \varepsilon f_i^{(2)}) \tag{13}$$

and the LBGK equation:

$$f_i(\mathbf{x} + \mathbf{e}_i, t+1) = f_i(\mathbf{x}, t) - \frac{f_i - f_i^{eq}}{\tau} \tag{14}$$

This LBGK equation can be broken down into two steps – collision and streaming – as follows:

The distribution functions f_i at the position $\mathbf{x}$, undergo collision by:

$$\tilde{f}_i(\mathbf{x}_i, t+1) = (1 - \frac{1}{\tau}) f_i(\mathbf{x}_i, t) - \frac{1}{\tau} f_i^{eq}(\mathbf{x}_i, t) \tag{15}$$

where, $\tilde{f}_i$ is the post collision state and $\mathbf{x}_i$ is a point in the discretized physical space.

Post collision, the distribution function, $\tilde{f}_i$ moves to the next location $\mathbf{x}+\mathbf{e}_i$ as:

$$f_i(\mathbf{x}+\mathbf{e}_i, t+1) = \tilde{f}_i(\mathbf{x}, t+1) \tag{16}$$

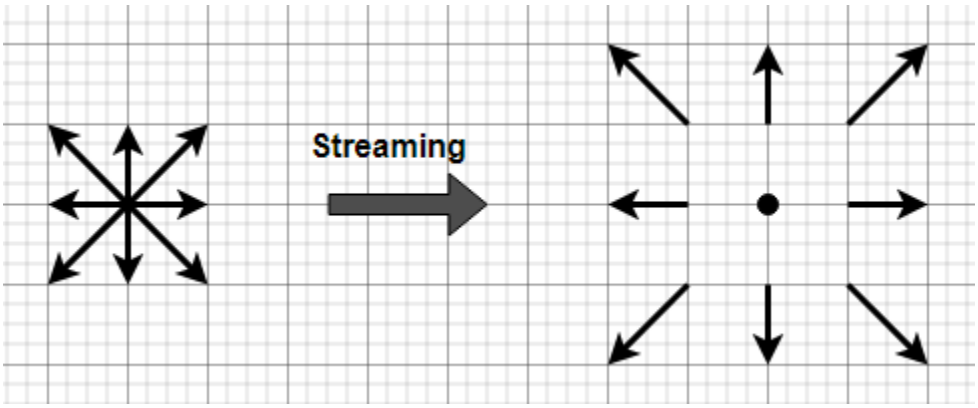

Figure 2.1 Streaming step

Relaxation time 'τ' has a complex relationship with the distribution function f and its value is assigned to be '1' for the flow solver, in the current work, due to stability considerations [10]. The kinematic viscosity is computed based on this relaxation time. Although the BGK type single relaxation time process in the kinetic equation allows for the recovery of the non-linear convection term in the Navier-Stokes equation through the multi-scale expansion, there have been claims that the multi-relaxation scheme offers better results with more stability and accuracy [11]. And as such, the MRT scheme has been applied to the flow solver.

Using the continuum form of the kinetic equation as given by (5) to the zeroth order in ε we can write the first order equation as:

$$\frac{\partial f_i^{(1)}}{\partial t_2} + \left(1 - \frac{2}{\tau}\right)\left[\frac{\partial f_i^{(1)}}{\partial t_1} + \mathbf{e}_i \cdot \frac{\partial}{\partial x_{1_i}} f_i^{(1)}\right] = -\frac{f_i^{(2)}}{\tau} \tag{17}$$

The mass and momentum conservation is hence derived, accurate to second order in ε:

$$\frac{\partial \rho}{\partial t} + \nabla \cdot \rho \mathbf{u} = 0 \qquad \text{and} \qquad \frac{\partial \rho \mathbf{u}}{\partial t} + \nabla \cdot \overline{\overline{\Pi}} = 0 \tag{18}$$

Here, Π is the momentum flux tensor and has the form:

$$\Pi_{\alpha\beta} = \sum_i (\mathbf{e}_i)_\alpha (\mathbf{e}_i)_\beta \left[f_i^{eq} + \left(1 - \frac{1}{2\tau}\right) f_i^{(1)} \right] \tag{19}$$

where, $(\mathbf{e}_i)_\alpha$ is the component of velocity vector $\mathbf{e}_i$ in the α direction.

2.3 D2Q9 lattice

For the two-dimensional square lattice with nine velocities, D2Q9, the values of $\mathbf{e}_i$ are as follows:

$$\mathbf{e}_i = \begin{cases} (0,0) & i = 0 \\ \left(\cos[(i-1)\pi/2], \sin[(i-1)\pi/2]\right) & i = 1,3,5,7 \\ \left(\cos[(i-1)\pi/2 + \pi/4], \sin[(i-1)\pi/2 + \pi/4]\right)\sqrt{2} & i = 2,4,6,8 \end{cases} \tag{20}$$

The lattice velocities in cartesian co-ordinates can be given as:

$$\begin{aligned} &\mathbf{e}_0 = 0, \\ &\mathbf{e}_1 = \hat{i}, \quad \mathbf{e}_2 = \hat{j}, \quad \mathbf{e}_3 = -\hat{i}, \quad \mathbf{e}_4 = -\hat{j}, \\ &\mathbf{e}_5 = \hat{i} + \hat{j}, \quad \mathbf{e}_6 = -\hat{i} + \hat{j}, \quad \mathbf{e}_7 = -\hat{i} - \hat{j}, \quad \mathbf{e}_8 = \hat{i} - \hat{j} \end{aligned} \tag{21}$$

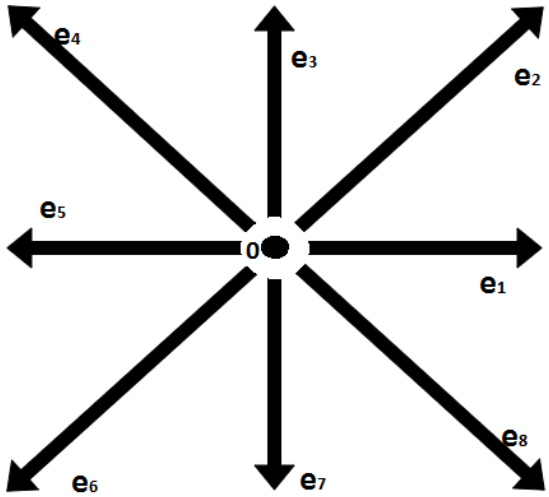

Figure 2.2 D2Q9 lattice

The equilibrium distribution function up to the second order is:

$$f_i^{eq} = \rho w_i \left[1 + 3\mathbf{e}_i \cdot \mathbf{u} + \frac{9}{2}(\mathbf{e}_i \cdot \mathbf{u})^2 - \frac{3}{2}u^2 \right] \tag{22}$$

with the values of weighting functions w_i given as:

$$w_i = \begin{cases} 4/9 & i = 0 \\ 1/9 & i = 1,3,5,7 \\ 1/36 & i = 2,4,6,8 \end{cases} \tag{23}$$

Using equations (22) and (23), the momentum flux tensor becomes:

$$\begin{aligned} \Pi_{\alpha\beta}^{(0)} &= \sum_i (\mathbf{e}_i)_\alpha (\mathbf{e}_i)_\beta f_i^{eq} = p\delta_{\alpha\beta} + \rho u_\alpha u_\beta, \\ \Pi_{\alpha\beta}^{(1)} &= \left(1 - \frac{1}{2\tau}\right) \sum_i (\mathbf{e}_i)_\alpha (\mathbf{e}_i)_\beta f_i^{(1)} = \nu(\partial_\alpha(\rho \mathbf{u}_\beta) + \partial_\beta(\rho \mathbf{u}_\alpha)) \end{aligned} \tag{24}$$

Where $p = \rho/3$ is the pressure, which gives the value of sound speed as a constant, $C_s = 1/\sqrt{3}$ and kinematic viscosity as $\nu = (2\tau - 1)/6$.

The resulting momentum equation is

$$\rho\left(\frac{\partial \mathbf{u}_\alpha}{\partial t}+\partial_\beta\cdot\mathbf{u}_\alpha\mathbf{u}_\beta\right)=-\partial_\alpha p+\nu\partial_\beta\cdot\left(\partial_\alpha\rho\mathbf{u}_\beta+\partial_\beta\rho\mathbf{u}_\alpha\right) \tag{25}$$

The Navier-Stokes equation is the same for small density variations.

2.4 D2Q4 lattice for temperature distribution

It has been well established that fluid flow problems, because of the advection term, require D2Q9 lattice arrangement as it ensures the macroscopic isotropy [11]. However, for temperature distribution, the D2Q4 lattice is sufficient because the diffusion phenomenon has no directional preference.

The LBGK equation for this lattice is the same as equation 14,

$$g_i(\mathbf{x}+\mathbf{e}_i,t+1)=g_i(\mathbf{x},t)-\frac{g_i-g_i^{eq}}{\tau} \tag{26}$$

but the velocities assume a different form:

$$\mathbf{e}_i=\sin(i\cdot\pi/2)+\cos(i\cdot\pi/2) \qquad i=1,2,3,4, \tag{27}$$

with the equilibrium distribution function taking the following form:

$$g_i^{eq}=w_iT(x,t)\left[1+3\mathbf{e}_i\cdot\mathbf{u}\right] \tag{28}$$

And the values of weighting function as:

$$w_i=1/4 \qquad i=1,2,3,4 \tag{29}$$

The macroscopic temperature is recovered in terms of the distribution function as:

$$T=\sum_i g_i \tag{30}$$

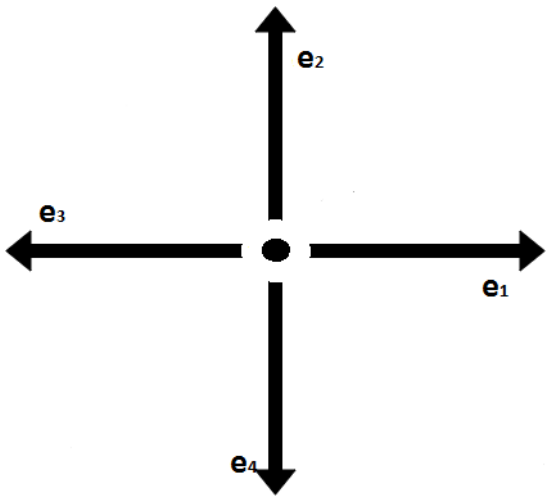

Figure 2.3 D2Q4 lattice

Next comes the question of the implementation of regeneration into the code, which is done by the means of a source term addition to the collision operator. Temperature and species field each have their own distribution functions and a source term needs to be added to each of them – to simulate conjugate heat transfer through the substrates in the temperature field and to simulate oxidation of soot in the species field.

2.5 Source term

The source term can be added to LBGK equation, in cases where there is an external force acting, as follows:

$$f_i(\mathbf{x}+\mathbf{e}_i, t+1) = f_i(\mathbf{x}, t) - \frac{f_i(\mathbf{x}, t) - f_i^{eq}(\mathbf{x}, t)}{\tau} + F_i \tag{31}$$

F_i can be defined as:

$$F_i = w_i \cdot \mathbf{F} \tag{32}$$

Where, w_i is the weighting function for the respective lattice structure used and **F** could be, for instance, the gravitational force with constant density flows. Alternatively, F could be the rate of heat generation due to a chemical reaction that is added to the LBE for temperature field.

2.6 Incompressible LB equation

The Lattice Boltzmann Equation is often used for incompressible flows, but the standard form of LBE recovers the compressible Navier-Stokes equations in the low Mach number limit. This problem led to the several efforts made by the various researchers towards a truly incompressible LBE. He & Luo proposed a LBGK model for incompressible Navier-Stokes equation [12]. Though widely accepted, He & Luo's model was succeeded by a new model, which replaced the older local pressure distribution function with a new equilibrium distribution function.

Guo et al. [13], in their work have designed a complete scheme for the recovery of the unsteady incompressible N-S equation, for which the equilibrium distribution function is defined as follows:

$$f_i^{eq} = \begin{cases} -4\sigma p + S_i(\mathbf{u}), & i = 0 \\ \lambda p + S_i(\mathbf{u}), & i = 1,2,3,4 \\ \gamma p + S_i(\mathbf{u}), & i = 5,6,7,8 \end{cases} \tag{33}$$

Where,

$$S_i(\mathbf{u}) = w_i \left[3(\mathbf{e}_i \cdot \mathbf{u}) + \frac{9}{2}(\mathbf{e}_i \cdot \mathbf{u})^2 - \frac{3}{2}(\mathbf{u} \cdot \mathbf{u}) \right] \tag{34}$$

and the three parameters, σ, λ and γ are governed by the following two equations:

$$\lambda + \gamma = \sigma, \qquad 2\lambda + 4\gamma = 1 \tag{35}$$

While Guo et al. attributed certain values for these three parameters after numerical tests, questions exist about alternate possibilities.

Murdock et al. [14] have derived an incompressible LBE of their own. They describe the equilibrium distribution function as:

$$f_i^{eq} = \begin{cases} 1 - 5p/3 + S_i(\mathbf{u}), & i = 0 \\ p/3 + S_i(\mathbf{u}), & i = 1,2,3,4 \\ p/12 + S_i(\mathbf{u}), & i = 5,6,7,8 \end{cases} \quad (36)$$

where, $S_i(\mathbf{u})$ has the same value as that in Guo's model (equation (34)). The weighting function, w_i, has the same value as that in the standard LBE scheme (equation (23)).

Equation (36) leads to the pressure equation:

$$p = -\frac{1}{5}\left[2(\mathbf{u}\cdot\mathbf{u}) + 3f_0^{eq} + 3\right] \quad (37)$$

A Chapman-Enskog expansion will yield the incompressible mass and momentum equations, and a viscosity value $\nu = \frac{1}{3}(\tau - 0.5)\Delta t$.

2.7 Boundary conditions

Like in any other CFD technique, boundary conditions play a critical role in Lattice Boltzmann method. As mentioned earlier in this report, the LBE has two steps – collision and streaming. The boundary conditions for LBE can be perceived as a special case of collision where a solid particle collides with a fluid particle. The distribution function, after streaming, is formulated into two divisions in the case of collision with a boundary – incoming and outgoing. The outgoing quantities are unknown and are a function of the incoming quantities and some other known quantities.

The figure 2-4 below shows the lattice velocities for the D2Q9 lattice with 9 velocities. If we consider this lattice's collision with the north wall then f_2, f_5 *and* f_6 are the incoming quantities and f_4, f_7 *and* f_8 are the outgoing quantities.

The boundary conditions can be categorized under two labels: Heuristic and Hydrodynamic. The sub-sections that follow will describe the various boundary conditions in detail.

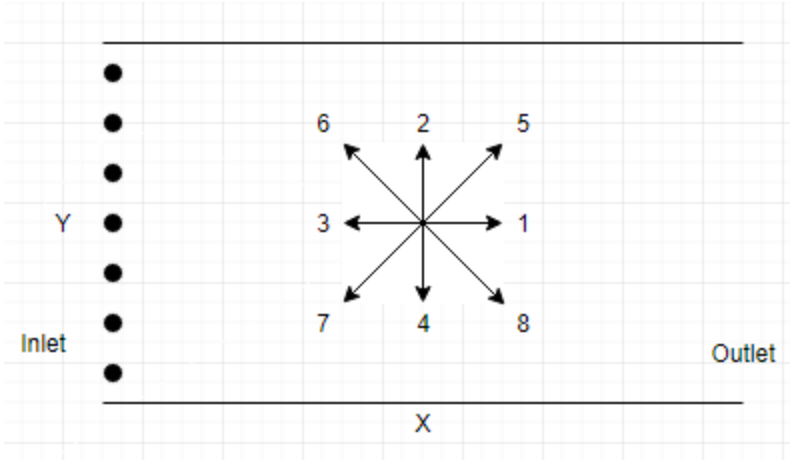

Figure 2.4 Discrete velocities of the D2Q9 lattice

2.7.1 Periodic boundaries

Periodic boundary conditions work by secluding bulk phenomena from the physical boundaries and hence are generally used in the cases where surface effects do not play any substantial role [15].

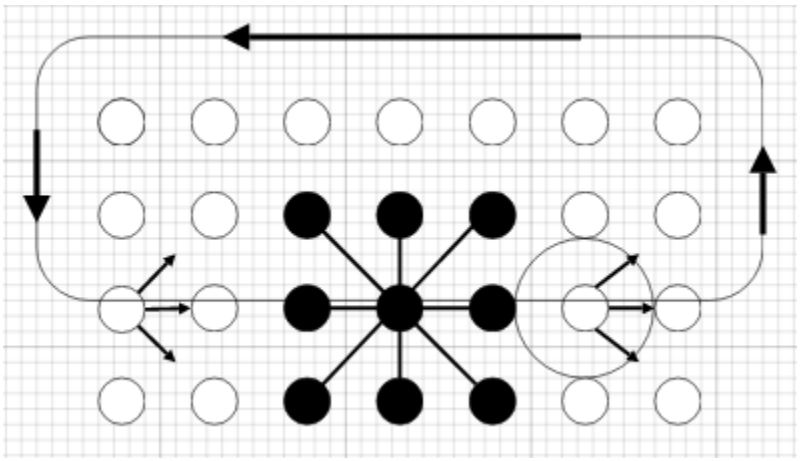

Figure 2.5 Periodic boundary condition schematic [15]

Above figure depicts the working of the periodic boundaries where the neighboring nodes of the boundary nodes are the boundary nodes on the opposite side. Also, the particles leaving the buffer on the right fill into the buffer on the left.

2.7.2 No-slip (bounce back) boundaries

According to this boundary condition, the fluid velocity at a given solid surface is zero, for cases where the solid surface has enough roughness to stop all fluid motion on it. There are two methods of implementation for this boundary condition that are discussed below.

2.7.2.1 On-grid bounce back, no slip

For the D2Q9 lattice in Figure 2.4, if the solid nodes are considered to be right on the north wall,

The equation for the on-grid bounce back boundary condition [15]:

$$\begin{Bmatrix} f_7 \\ f_4 \\ f_8 \end{Bmatrix} = \begin{bmatrix} 1 & 0 & 0 \\ 0 & 1 & 0 \\ 0 & 0 & 1 \end{bmatrix} \begin{Bmatrix} f_5 \\ f_2 \\ f_6 \end{Bmatrix} \tag{38}$$

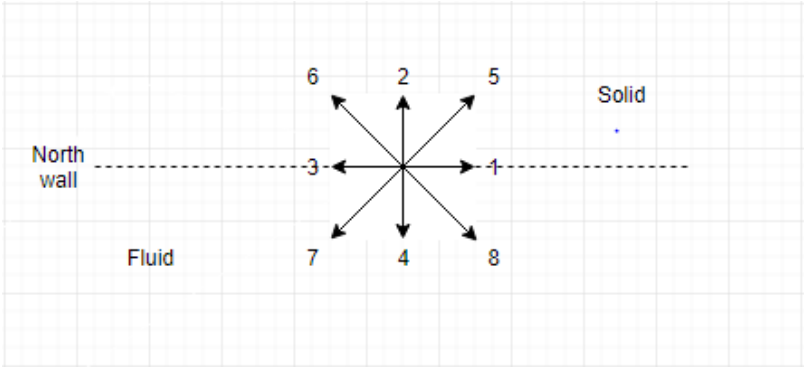

Figure 2.6 On grid bounce back [16]

2.7.2.2 Mid-grid bounce back, no slip

The on-grid bounce-back gives only first-order accuracy because the streaming operator at the boundary has a one-sided character. If we use mid-line reflection, we can have second-order

accuracy, but with certain complications in implementation. Care must be taken in handling the corner nodes while implementing mid-grid bounce-back.

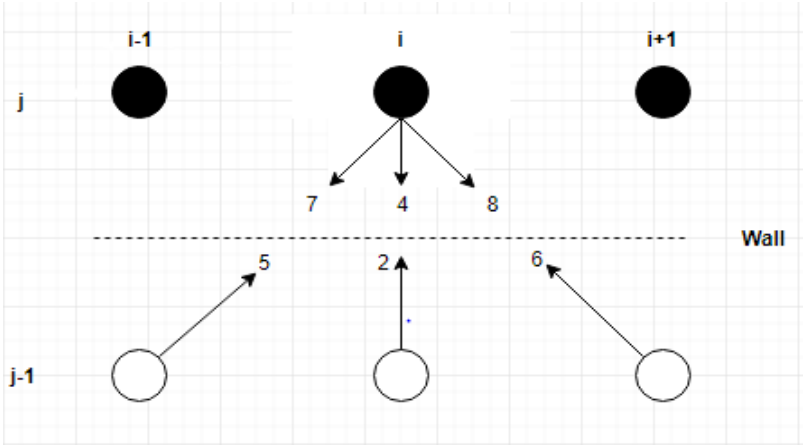

Figure 2.7 Mid-grid bounce back

The distribution functions are given by:

$$\begin{Bmatrix} f_7(i,j) \\ f_4(i,j) \\ f_8(i,j) \end{Bmatrix} = \begin{bmatrix} 1 & 0 & 0 \\ 0 & 1 & 0 \\ 0 & 0 & 1 \end{bmatrix} \begin{Bmatrix} f_5(i-1,j-1) \\ f_2(i,j-1) \\ f_6(i+1,j-1) \end{Bmatrix} \tag{39}$$

2.7.3 Free-slip boundaries

Free slip boundaries are for smooth walls with almost no friction applied on the fluid. There is no tangential momentum exchange between the wall and fluids. The reflection of velocities is specular implying that the mean of incoming and outgoing velocities is zero. There are again two methods of implementation – On-grid and Mid-grid.

The equation for on-grid being:

$$\begin{Bmatrix} f_7 \\ f_4 \\ f_8 \end{Bmatrix} = \begin{bmatrix} 0 & 0 & 1 \\ 0 & 1 & 0 \\ 1 & 0 & 0 \end{bmatrix} \begin{Bmatrix} f_5 \\ f_2 \\ f_6 \end{Bmatrix} \tag{40}$$

And mid-grid:

$$\begin{Bmatrix} f_7(i,j) \\ f_4(i,j) \\ f_8(i,j) \end{Bmatrix} = \begin{bmatrix} 0 & 0 & 1 \\ 0 & 1 & 0 \\ 1 & 0 & 0 \end{bmatrix} \begin{Bmatrix} f_5(i-1,j-1) \\ f_2(i,j-1) \\ f_6(i+1,j-1) \end{Bmatrix}. \tag{41}$$

2.7.4 Von Neumann (flux) boundaries

Von Neumann boundary condition is hydrodynamic type of boundary condition. This kind of boundary condition constricts the flux (for example, heat or momentum flux) to a constant value at the boundaries. If applied on momentum flux, it can be used as velocity boundary conditions. In Figure 2.4, if we consider the node on the south wall, the unknowns f_5, f_2, f_6 *and* ρ are calculated based on the conditions inside the domain with $\mathbf{u}_{wall} = u_{x,swall}\hat{i} + u_{y,swall}\hat{j}$ [17]. The unknown distribution functions are computed from equation (3) to be:

$$\begin{aligned} f_2 &= f_4 + \frac{2}{3}\rho u_{y,swall} \\ f_5 &= f_7 - \frac{1}{2}(f_1 - f_3) + \frac{1}{2}\rho u_{x,swall} + \frac{1}{6}\rho u_{y,swall} \\ f_6 &= f_8 - \frac{1}{2}(f_1 - f_3) - \frac{1}{2}\rho u_{x,swall} + \frac{1}{6}\rho u_{y,swall} \end{aligned} \tag{42}$$

where,

$$\rho = \frac{1}{1-u_{y,swall}}\left[f_0 + f_1 + f_3 + 2(f_4 + f_7 + f_8)\right] \tag{43}$$

And the assumption is that the bounce back rule holds for the non-equilibrium part of the particle distribution which is normal to the boundary.

2.7.5 Dirichlet boundaries

Another hydrodynamic boundary condition, the Dirichlet boundary considers the pressure/density to be constant at the boundaries. Once again considering Figure 2.4 for the inlet boundary, the unknowns here are the distribution functions $f_1, f_5 \, and \, f_8$ and the inlet flow velocity $u_{x,in}$. The density and inlet y-velocity, $\rho = \rho_{in}$ and $u_{y,in} = 0$ are specified.

The unknowns are then computed to be:

$$u_{x,in} = 1 - \frac{\left[f_0 + f_2 + f_4 + 2(f_3 + f_6 + f_7) \right]}{\rho_{in}} \tag{44}$$

$$f_1 = f_3 + \frac{2}{3} \rho_{in} u_{x,in} \tag{45}$$

$$f_5 = f_7 - \frac{1}{2}(f_2 - f_4) + \frac{1}{6} \rho_{in} u_{x,in} \tag{46}$$

and,

$$f_8 = f_6 + \frac{1}{2}(f_2 - f_4) + \frac{1}{6} \rho_{in} u_{x,in} \tag{47}$$

Also, the same bounce back rule assumption holds for the parts of the particle distribution normal to the boundary.

2.8 Unit System in Lattice Boltzmann Method

Lattice Boltzmann has its own system of units which is dimensionless. Conversion from physical units to LB units is a two-step process and involves the use of dimensionless numbers like Reynolds and Prandtl. A step-wise conversion process is presented in this section.

For any physical quantity, Q, an expression of the following form can be written:

$$Q = C_Q \cdot \tilde{Q} \tag{48}$$

where, Q is the physical quantity with units, C_Q is the conversion factor and $\tilde{Q}$ is the non-dimensional equivalent of the quantity in LB units. Following are the steps explaining the conversion from physical units to LB:

1. Recognize all the physical quantities involved in a problem including, but not limited to, viscosity, dimensions of the domain, flow velocity etc.
2. Compute all the non-dimensional numbers required (Reynold's number (*Re*), Prandtl number (*Pr*), etc.)
3. Next, we choose any two dimensionless LB parameters, like characteristic length ($\tilde{H}$) and relaxation time ($\tilde{\tau}$).
4. For convenience, the LB space and time steps ($\Delta x, \Delta t$) are chosen to be unity. This leaves us with $\Delta x = C_H$ and $\Delta t = C_t$. The LB value of density ($\tilde{\rho}$) is arbitrarily set to 1.
5. Viscosity has the following expression:

$$\nu = \left(\tau - \frac{1}{2}\right) c_s^2 \Delta t \tag{49}$$

   This leads to the time conversion factor:

$$\begin{aligned} \nu &= \frac{\left(\tau - \frac{1}{2}\right)}{3} \frac{C_H}{C_t} \\ \Rightarrow C_t &= \frac{\tau - \frac{1}{2}}{3} \frac{C_H}{\nu} \end{aligned} \tag{50}$$

6. The dimensionless numbers, Reynold's (*Re*), Prandtl (*Pr*), have the same value in both systems (physical and LB) of units. Hence, $\mathrm{Re} = \tilde{\mathrm{Re}}$ and this gives us:

$$\frac{\nu}{u_m H} = \frac{\tilde{\nu}}{\tilde{u}_m \tilde{H}}, \quad \therefore\ C_\nu = C_u C_H \tag{51}$$

where, C_ν, C_u and C_H are the conversion factor for viscosity, velocity and length respectively.

7. The primary conversion factors found in the previous steps can be now used to find the secondary conversion factors like C_u:

$$C_u = \frac{C_H}{Ct} \tag{52}$$

   And hence, the maximum lattice velocity:

$$\tilde{u}_m = \frac{u}{C_u} \tag{53}$$

8. Verify the conversion by balancing the dimensionless number, Reynold's number in this case, between the physical and the LB units.
9. Check for the validity of the converted values for LBM. For example, the converted value of maximum lattice velocity, $\tilde{u}_m$, must be less than 0.3 in conjunction with the low Mach number limit.
10. Repeat steps 3 through 9 until a valid a set of consistent and valid LB values is found.

If one was to start with two different parameters, for example, $\tilde{H}$ and $\tilde{u}_m$ or $\tilde{u}_m$ and τ, the set of values derived at the end would be entirely unique but equally correct.

3 Diesel Particulate Filters

Diesel Particulate Filters have been in use for Particulate Matter emission control for almost three decades and have proven to be one of the most effective methods of exhaust after treatment in diesel engines. The after-treatment technologies can be classified into two major types – filtering and non-filtering [18]. The filtering type devices essentially make use of a mesh-like trap structure, located in the under-floor exhaust line, to collect the soot particles which are the major components of the particulate matter. The non-filtering type devices make use of catalytic compounds to oxidize the carbon monoxide and hydrocarbons present in the soluble organic fraction (SOF) of the PM. Diesel oxidation catalysts (DOC), as the non-filtering type methods are popularly known, are not efficient at reducing soot (which is the major component of PM) and are used in combination with the traps (filtering type). This device is collectively known as the honeycomb-monolithic catalytic conversion. All these devices operate mostly through inertial impaction, interception or diffusion mechanisms. There is essentially a two-step mechanism to all the modern diesel particulate filters. First is the trapping of the particulate matter and second is the regeneration process, which is essentially the cleaning process applied to get rid of the trapped soot with or without the help of catalytic compounds.

The filtering systems consist of a trap capable of collecting the particulate matter. These traps can make use of three types of media, namely:

1. Ceramic monoliths (Wall-flow filters)

2. Ceramic or metallic yarns (Fiber type partial filters)

3. Ceramic of metallic foams (Foam type partial filters)

Wall-flow filters are the most efficient. This type of filters can be called ‘cake’ type filters because the soot collected by these filters gets caked on them over time. The partial filters on the other hand can be called ‘deep-bed’ filters as they make use of a porous filtration medium to retain the particles collected [19]. The materials used to create the

traps can be partially sintered SiC or cordierite grains (pore size: 10 μm) for wall-flow filters, zirconia-toughened-alumina or mullite, SiC (pore size: 100–400 μm) for foam type partial filters, doped-alumina (fiber size: 10 μm) for fiber type partial filters [20]. The Diesel oxidation catalysts are sometimes used in combination with these traps, placed just before or after the actual trap or the catalysts could be deposited directly on the traps. This is done to further improve the efficiency of the pollution control device.

The most effective and popular type of DPF, the Wall-flow filters, make use of the ceramic monoliths which get laden by particulates. This is true for all types of traps and is the root cause behind the need of employing trap regeneration techniques. The traps, when laden with particulates, are clogged and this causes an increase in pressure drop across them, which levies a high fuel penalty. To rectify this problem, a layer of catalysts is deposited on the wall-flow monolith, which oxidizes the deposited soot.

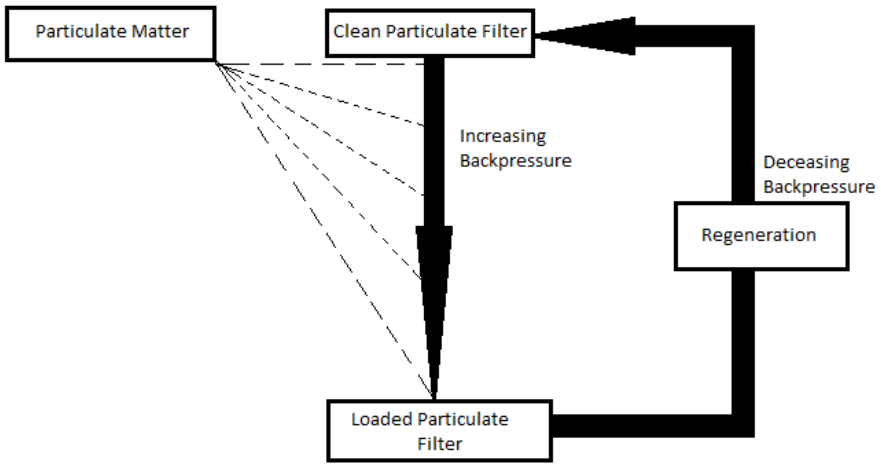

Figure 3.1 Diesel Particulate Filter operation schematic.

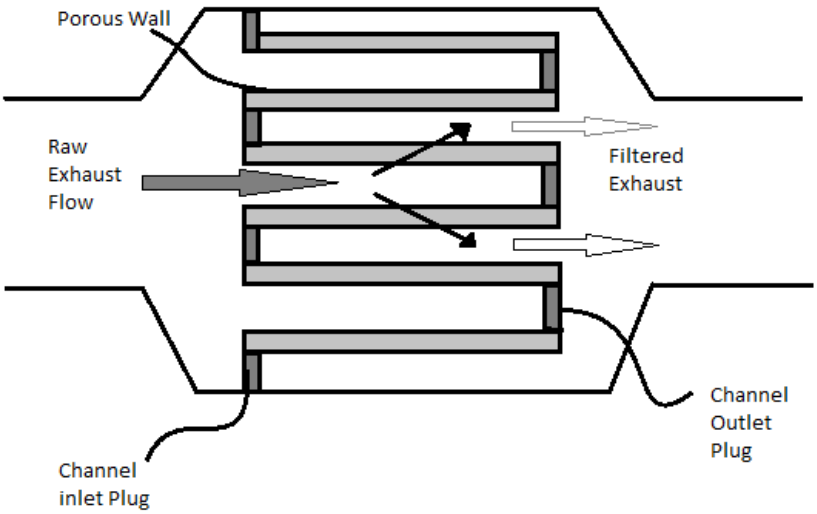

Figure 3.2 Wall-flow filter schematic - channels greatly exaggerated.

Figure 3.2 above shows the schematic of a wall flow filter. This type of filter is essentially an extrudate made of the synthetic ceramic cordierite or silicon carbide material, to form numerous axial channels, typically of square cross section, which are blocked at alternate ends in a way which forces the exhaust gases coming in to go through the porous substrate walls which act as a mechanical filter [19].

The porous nature of the filtering technique makes it a suitable candidate for an LBM analysis and has been discussed at length in previous works [10].

As discussed above, regeneration is the cleaning of the DPF traps after the soot has been collected on them to avoid clogging and therefore the back-pressure drop through filter and that it is the second step in the two-step mechanism of PM after-treatment. Diesel particulate filters go through spontaneous combustion in air in the temperature range of 500-600^{o} C [20]. So, the problem facing the automotive after-treatment of PM through DPF is achieving these temperatures at a constant rate for sufficient amounts of time in diesel vehicles which is not typically the case. Apart from the obvious reasons behind wanting to burn off the trapped particulates, there is also the fact that excessive collection of soot on the trap may lead to back-pressure increase and therefore exhaust gas temperature increases up to the point where it leads to a sudden burn-off, occasionally melting the trap itself. Hence, a term called ‘controlled regeneration’ is introduced. There

is a need to control the temperatures of the particulate filters to burn off the soot but preserve the filter material itself. This can be achieved by use of external means of raising the temperatures. The other option is to decrease the temperature of soot ignition by reacting it with catalysts.

Based on these deductions, the regeneration process can be classified into two categories:

1. Active regeneration

2. Passive regeneration

Before talking about the two methods separately, it is worth mentioning that a combination of the two techniques generates even better results and has been achieved by different car manufacturers over the world of which one has been discussed in this report.

Active regeneration is the name given to the external means used to raise the temperature of the exhaust gas or the trap itself up to the point of soot ignition, which is a more direct method of soot 'burn-off'.

Active regeneration can be achieved by three different means: fuel additives, electric heating of trap or heating of trap using a burner. Exhaust can be post-injected with a combustible additive, or fuel itself, upstream the trap which ignites and releases heat thereby increasing the temperature of the exhaust gases. Injection of catalysts or reactive species just before the exhaust enters the trap is also an option. Electric heating of traps is done by incorporating heating wires in the filters during manufacturing or by heating it by means of microwaves when using a conductive material. Alternatively, for heating the filter by a burner a dual filter mechanism is developed in which one filter is 'online' to collect the particulates while the other is 'off-line' for regeneration by burner.

Passive regeneration employees a variety of chemicals used as catalysts to speed up the soot oxidation. Fuel borne catalytic conversion involves a continuous supply of catalysts in the fuel. Commercially available regeneration promoting fuel-borne catalysts are based on Cerium, Copper, Iron, Platinum, Strontium and Sodium fuel-soluble compounds. Fleet

operations can facilitate the dropping of the catalytic compounds in the central fuel tank, while individual vehicle applications call for an on-board, controlled dosing system. Catalytic filter coatings are essentially traps (popularly honeycomb mesh) coated with the catalytic chemicals. Catalyst contact is crucial in filter coatings for proper oxidation which is achieved by use of washcoats. NO_2 generation through catalytic oxidation of nitrogen oxide is another means of passive regeneration. Nitrogen di-oxide can be a much more effective oxidizer for soot.

The numerical simulation of transport, deposition and oxidation (regeneration) of soot, as related to the current work, has been discussed in the chapter that follows.

4 Numerical Simulation

The algorithm for most of the framework for flow through disordered media with the LBM has been coded with the C language. Additionally, the code uses OpenMP for parallelization. The C language, in combination with the ease of parallelizing, possessed by OpenMP, provides the speed which is critical for massive simulations. The open source software Paraview along with the Michigan Technological University licensed software Tecplot is used for post processing.

4.1 Porous Media Generation Simulation

The inner porous structure of the filter wall is simulated using the random number generator feature of the C language which accepts several seed sites and min./max. size intervals. This approach ensures better control of the substrate properties like porosity, wetted surface area etc. The basic shape of the substrate blockages is assumed to be an ellipse. The number of seed sites determines the porosity of the filter. The min./max. size determines the size of the major and minor axes of the ellipse. These two parameters, in combination, form a complex geometry that mimics the filter substrate wall.

In the following piece of code, the variables num1 and num2 are the randomly generated x and y coordinates for the substrate position and the variables Rp1 and Rp2 are the random ellipse axis size between the allowable limits. So, ellipses of random minor and major axes are built around randomly selected seed sites and some of these structures will overlap as the porosity increases, to provide a more complex geometry. The second part of the code shows the variable ‘rp’ which defines the equation of an ellipse with the four random variables generated above and sets the nodes within this ellipse to be solid. Grid sensitivity studies were conducted to reveal the ideal grids and ellipse extents – for porosities greater than 0.7, a grid size of 302×401 and for porosities less than 0.7 a grid size of 302×601 is determined to be ideal [21].

```
for(b=0;b<bmax;b++)
{
    num1=(rand()%filter)+inlet;
    Rp2=(rand()%sizeseed)+sizeseed;

    num2=rand()%Ny;
    Rp1=(rand()%sizeseed)+sizeseed;

    for(j=0;j<=Ny;j++)
    {
        for(i=0;i<=Nx;i++)
        {
            rp=((i-num1)*(i-num1)/(Rp1*Rp1)+(j-num2)*(j-num2)/(Rp2*Rp2));
            if(rp<1.0)
            {
                nodes[j][i]=0;
                body[j][i]=0;
            }
        }
    }
}
```

This substrate generator model was verified by making use of two metrics – friction factor vs. Reynolds number (Ergun Hypothesis) for several porosities, and permeability vs. porosity for several velocities. The substrate generated for a porosity of 0.9 is shown in the following figure, where blue color demonstrates solid substrate.

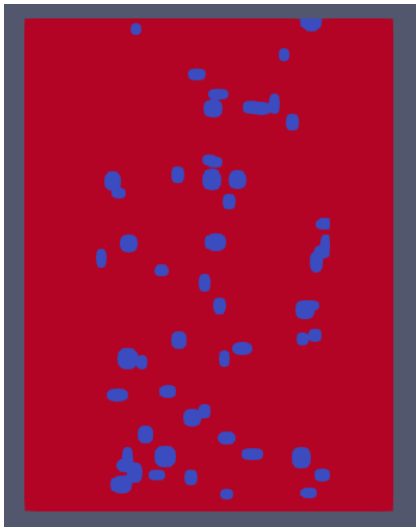

Figure 4.1 Generated substrate for porosity 0.9

4.2 Deposition

To simulate the soot deposition on filter substrate, a deposition probability or a probability of sticking, P_s, is defined. Yamamoto et al. [22] conducted a parametric study over a wide range of P_s. They define the deposition model as follows: an area around the substrate is deposited with soot at a given time. At the next time step, the soot is transported by the flow to the next lattice point. At this node, the soot is deposited depending upon the sticking probability P_s. If the incoming soot falls on the node at a probability of $(1-P_s)$, it is not deposited and is rebounded into the flow and transported again. Due to the deposition, the soot concentration at the given node keeps adding up and eventually the soot mass fraction becomes unity. Once this happens, this node is redefined to be a solid deposited node as opposed to the previously defined gas phase node and streaming stops at this node. And, the lattice point ahead of the newly deposited node is now observed for the soot concentration addition. Thus, the soot deposition layer grows. The piece of code below shows the implementation of the above explained phenomena.

```
if(shape[j][i]==1)
{
    Y2[j][i]+=Ps*Y[j][i];
    Y[j][i]-=Ps*Y[j][i];
}

if(Y2[j][i]>=1.0)
{
    nodes[j][i]=0;
    Y2[j][i]=1.0;
    Y[j][i]=0.0;
    ux[j][i]=0.0;
    uy[j][i]=0.0;
}
```

Here, shape[j][i] represents whether the given node is a boundary node. Y2[j][i] and Y[j][i] represent the deposited and gas soot concentrations respectively. Once the deposited soot mass fraction becomes unity at a particular node, node[j][i] is set equal to be zero, which is the default value for solid nodes. The gas soot concentration becomes

zero as well at the given node and so does the velocity. A flow chart of the deposition model is presented below [1].

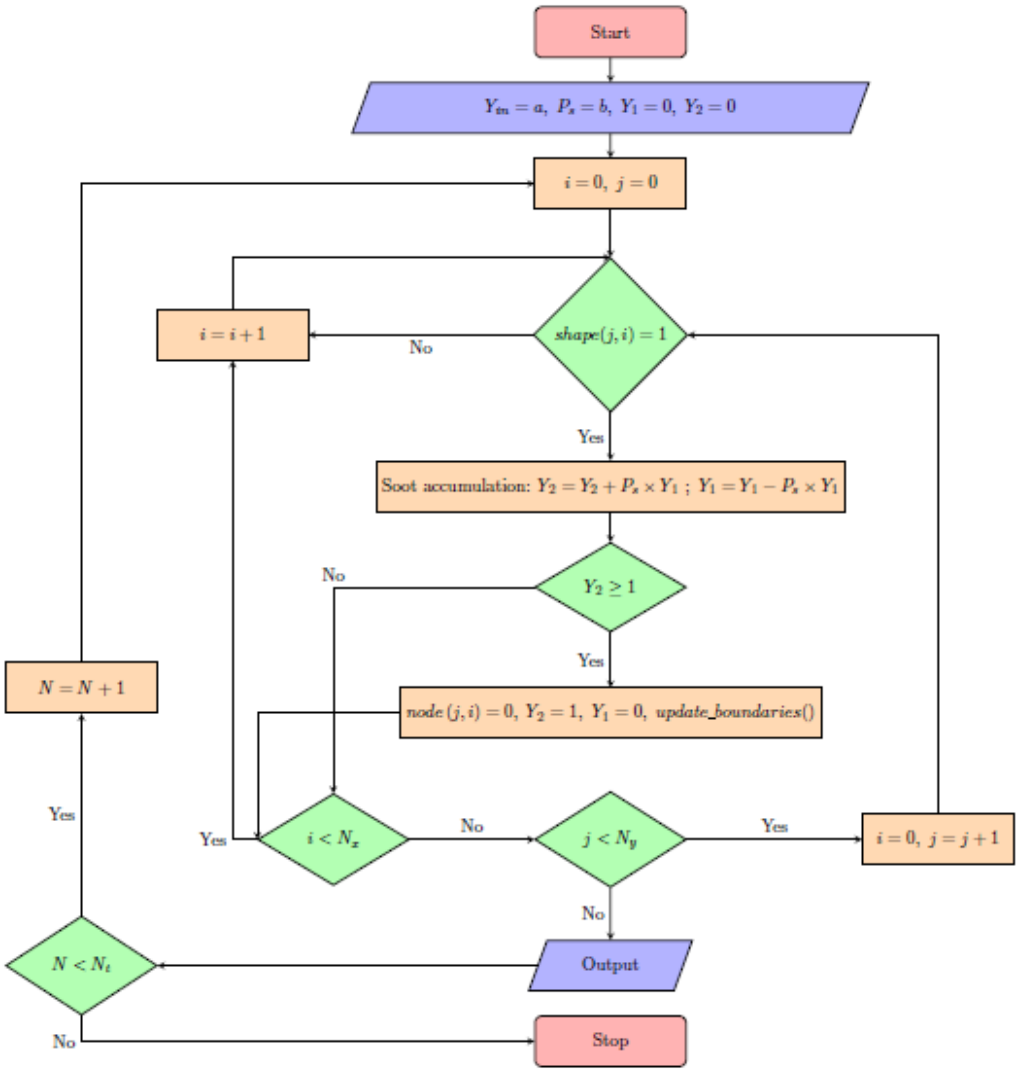

Figure 4.2 Algorithm for the deposition model

4.3 Regeneration

Regeneration of the diesel particulate filter is, as mentioned earlier in this report, the oxidation of the deposited soot. Although there has been a lot of research performed on the oxidation of soot – both catalytic and non-catalytic, the study of the detailed kinetics of soot oxidation has not been considered as much. In the absence of any conclusive study on actual diesel soot, most researchers have modeled soot for their studies with variations of carbon black, which is a substance resembling diesel soot in chemical properties including activation energy, pre-exponential factor and oxidation rate. Several researchers have studied Printex U – a flame soot produced by Degussa AG [23, 24]. Neeft, et al. [25] conducted one such important study, wherein they present the detailed properties of Printex U and its comparison with diesel soot. Printex U is essentially a form of carbon black and its oxidation can be represented by the following one-step global mechanism [23, 26]:

$$C + O_2 \rightarrow CO_2 \tag{54}$$

The rate of reaction of the above reaction will be given as:

$$r = k \cdot C_{soot} \cdot C_{oxygen} \tag{55}$$

where ‘k’ is the rate constant given by the Arrhenius law:

$$k = A \cdot e^{\left(\frac{-E_a}{RT}\right)} \tag{56}$$

In equation 55 above, the global reaction rate assumes the order of reaction to be ‘1’ for both participant species. C_{soot} and C_{oxygen} are the molar concentrations of the incoming soot and oxygen, and can be determined from their mass fractions in the incoming exhaust gas.

$$C_i = \frac{\rho_0 Y_i}{M_i} \tag{57}$$

where, ρ_0 is the constant density at room temperature and M_i are the molecular weights of the i[th] species of the reactants, carbon and oxygen in this case [27].

This brings us to the species production rate defined by Yamamoto et al. [27]:

$$\begin{aligned} \omega_i &= a_i \cdot M_i \cdot r \\ &= a_i \cdot M_i \cdot A \cdot e^{\left(\frac{-E_a}{RT}\right)} \cdot \frac{\rho_0 Y_{soot}}{M_{soot}} \cdot \frac{\rho_0 Y_{oxygen}}{M_{oxygen}} \end{aligned} \tag{58}$$

a_i in the above equation are the stoichiometric coefficients - $a_{soot} = a_{oxygen} = -1$ in this case, since oxygen and soot are both being consumed.

The species production rate depends on two parameters – local temperature and the rate of reaction, which in turn depends upon the local species concentrations. The LBE's for the species make use of the two-dimensional lattice with 9 velocities similar to the flow field and are represented as $h_i(\mathbf{x}, t, \mathbf{u})$ (for soot) and $r_i(\mathbf{x}, t, \mathbf{u})$ (for oxygen concentration) in the code. The mass fraction of the species is calculated in terms of the distribution functions as:

$$Y_{soot} = \sum_i h_i \qquad \textit{and} \qquad Y_{oxygen} = \sum_i r_i \tag{59}$$

4.3.1 Implementation

The species production rate calculated in equation 58 above is added to the species collision operators as a source term, as discussed in the section 2.5 of chapter 2.

Now, since the species production rate described above is in fact, the soot oxidation rate in the present scenario, it bears a negative sign. Thus, the source term is being subtracted from the collision process for the species. As can be seen from equation 58 above, the species production rate and eventually the source term, for the collision operator depends on temperature due to the inclusion of the Arrhenius rate law. And, as discussed in chapter 3 above, the thermal or active regeneration of the filters involves raising the temperature of the DPF above the threshold value of spontaneous soot combustion. In

real world applications, this is achieved by injecting a small amount of a combustible additive, or fuel itself, upstream of the filter in the exhaust stream. This additive then combusts, thus raising the temperature above the threshold. For the purposes of this simulation, this rise in temperature is achieved by raising the inlet temperature defined at the beginning of the simulation. This rise in temperature is applied only after a certain time-step at which the soot cake layer formation can be clearly seen. In addition, the rise must be gradual so that it can mimic the real-world process. Both these conditions are achieved in the simulation by fitting in a quadratic curve for inlet temperature increase after the time-step where there is a visible soot cake layer observed because of which the pressure drop shoots up suddenly (due to the sudden drop in porosity, since the filter is totally blocked). The implementation is shown in the following code:

```
if(del_p>=0.15)
{
  Tin=0.01+1.25e-17*(number-kin)*(number-kin);
  if(Tin>0.015)
  Tin=0.015;
}
  else
  Tin=0.01;
```

Here, ‘Tin’ is the inlet temperature and ‘del_p is the pressure drop. The variable ‘number’ stores the increasing time steps and ‘kin’ is the first time-step after the pressure drop starts shooting up. Hence, ‘(number – kin)’ represents the effective time-step after regeneration starts. The quadratic equation depicted is designed to increase the temperature to the threshold value over the span of twenty million time-steps. After this point, the maximum filter temperature stays constant due to the addition of heat of combustion until the end of regeneration, which replicates the physical process with a high degree of accuracy.

It is only after the inlet temperature reaches the threshold value and then diffuses through the domain that the regeneration occurs. In other words, the addition of the source term on each node is restricted until the temperature at that node reaches the threshold value. The implementation of the above-described process gets tricky when one considers the

fact that the deposited nodes have been set to solid according to the model used by Yamamoto et al. [22]. The streaming process in the LBE for the species is restricted to the fluid nodes as there can be no transport of particles in the deposited region. In addition, the LBE is applied to the gas phase concentration of the soot (which is zero at the deposited nodes). Therefore, applying the source term at this point would not work as expected. Thus, we need a reversal of the deposition model discussed earlier, for the regeneration to work. Therefore, before applying the source term to the collision operator, we turn all the deposited nodes into fluid and turn the deposited concentration to gas phase concentration. This enables the implementation of the source term into the collision operator. The code that follows shows the implementation.

```
if(T[j][i]>=Tcut)
{
    if(nodes[j][i]==0)
    {
    nodes[j][i]=1;
    }
    if(Y2[j][i]>0)
    {
    Y[j][i]=Y2[j][i];
    Y2[j][i]=0.0;
    }

    HEQ=heq(Y[j][i],ux[j][i],uy[j][i],k);
    h_post[j][i][k]=h[j][i][k]-(h[j][i][k]-HEQ)/tauy -source;
}
else
{
    HEQ=heq(Y[j][i],ux[j][i],uy[j][i],k);
    h_post[j][i][k]=h[j][i][k]-(h[j][i][k]-HEQ)/tauy;
}
```

Here, the variable ‘source’ is the source term:

```
K=A*(exp(-EabyR/T[j][i]));
r=K*(rho*Y[j][i]/Msoot)*(rho*O[j][i]/Mo);
omega=Msoot*r;
source=w[k]*omega;
```

Where, ‘A’ is the Arrhenius constant and ‘EabyR’ is the activation energy divided by universal gas constant coupled into one term. ‘K’ is the rate constant according to the Arrhenius law. Msoot and Mo are the molecular weights of the species involved and ‘rho’ represents density. Rate of reaction for the soot oxidation is represented by ‘r’. Omega represents the species production rate. ‘w[k]’ is the array holding the weighting functions for the D2Q9 lattice used for the species solver.

T[j][i], Y[j][i] and O[j][i] are arrays holding the temperature, soot concentration and oxygen concentration respectively. The oxygen solver is modeled in a similar manner as the soot solver with the exception that there is no deposition, and therefore no reversal of it, involved. The relaxation time ‘tauy’ is calculated based on the diffusivity of the species through the domain. ‘Tcut’ is the threshold temperature at which the activation energy for soot oxidation is achieved.

The oxidation process increases the temperature of the DPF because of the generated heat of reaction. This heat of reaction varies with the soot oxidation rate at each time step and thus, the heat release calculated for the reaction given in equation 54 above is multiplied by the soot oxidation rate in equation 58 [27]. The heat release from the soot oxidation sets-off the conjugate heat transfer. This is also modeled into the temperature collision term through the addition of a source term. In the case of temperature, the source term is added, as the temperature is increasing due to the heat addition. This heat addition then takes over the temperature, and therefore, the regeneration process after the initial injection of combustible additives.

```
K=A*(exp(-EabyR/T[j][i]));
r=K*(rho*Y[j][i]/Msoot)*(rho*O[j][i]/Mo);
omega=Msoot*r;
source_t=wt[k]*qs*omega;
```

Here, ‘source_t’ represents the source term for temperature. ‘qs’ is the heat release from soot oxidation and ‘wt[k]’ is the array holding the weighting functions for the D2Q4 lattice used in the temperature solver.

The code below depicts the addition of the source term once the temperature has crossed the threshold value and oxidation has begun. The relaxation time ‘taut’ is calculated from the fluid thermal diffusivity value based on the Prandtl number and the viscosity. The relaxation time ‘tauts’ is calculated from the thermal diffusivity of the solid substrate, cordierite in this case.

```
if(nodes[j][i]==1)
{
  if(T[j][i]>=Tcut)
  {
    GEQ=geq(T[j][i],ux[j][i],uy[j][i],k);
    g_post[j][i][k]=g[j][i][k]-(g[j][i][k]-GEQ)/taut +source_t;
  }
  else
  {
    GEQ=geq(T[j][i],ux[j][i],uy[j][i],k);
    g_post[j][i][k]=g[j][i][k]-(g[j][i][k]-GEQ)/taut;
  }
}
else
{
  if(T[j][i]>=Tcut)
  {
    GEQ=geq(T[j][i],ux[j][i],uy[j][i],k);
    g_post[j][i][k]=g[j][i][k]-(g[j][i][k]-GEQ)/tauts +source_t;
  }
  else
  {
    GEQ=geq(T[j][i],ux[j][i],uy[j][i],k);
    g_post[j][i][k]=g[j][i][k]-(g[j][i][k]-GEQ)/tauts;
  }
}
```

A flow chart depicting the regeneration process is shown on the next page.

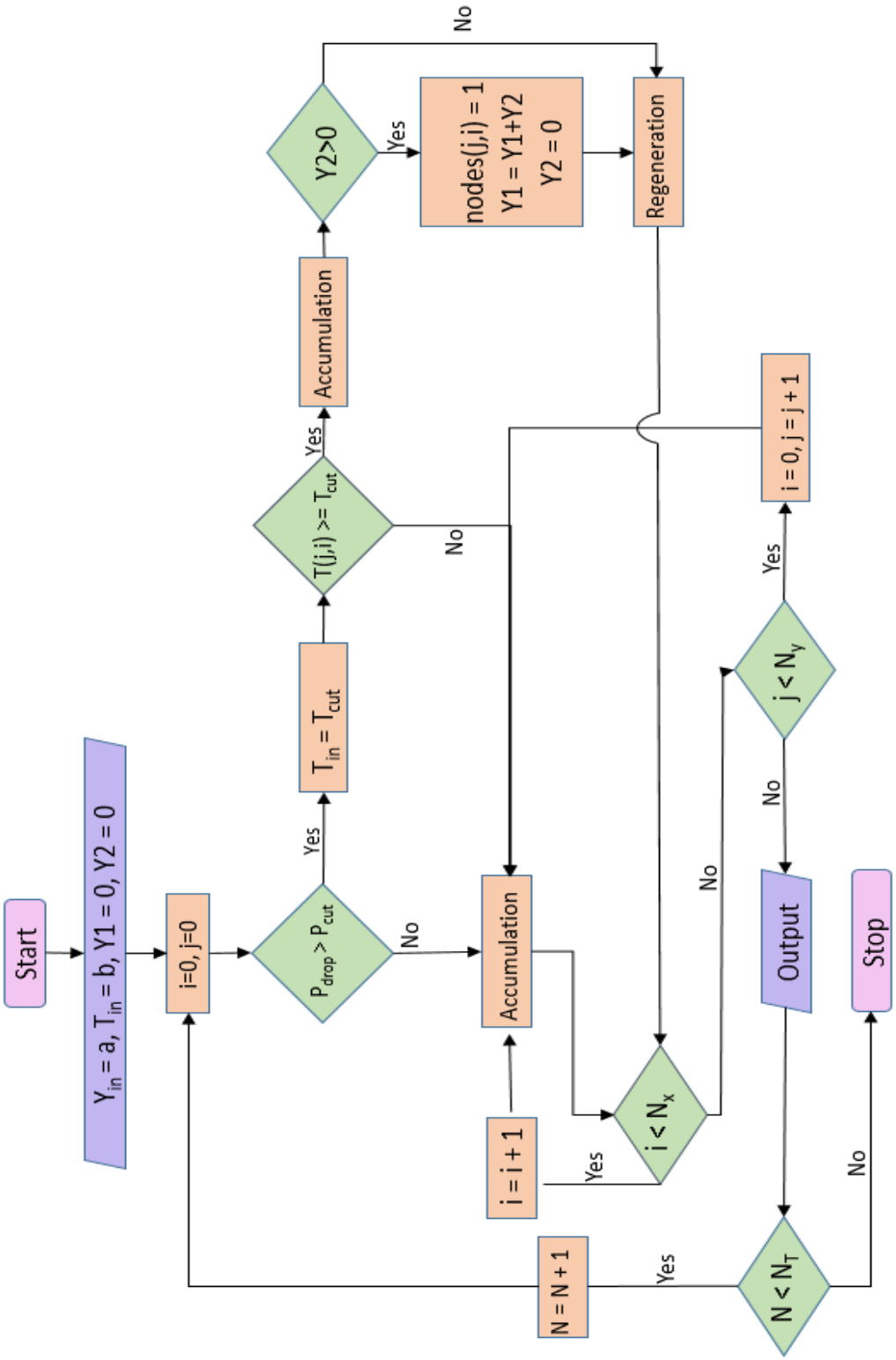

Figure 4.3 Flow-chart depicting the regeneration model algorithm

5 Results

Having discussed all the concepts thoroughly in the previous chapters, this chapter presents all the major results. The results are accompanied by a detailed discussion on the inferences that can be drawn from the said results.

5.1 Regeneration in flow over a cylinder

The deposition model of Yamamoto et al. was tested in earlier work [1] for the benchmark case of flow over a cylinder.

The current work also uses the same case for testing the regeneration model. The velocity and species solver work in the exact same way as described above for the porous media case and the results meet the expectations. The difference between the cylinder case and the case for DPFs is that the probability of sticking value is higher for the cylinder case. The value of P_s used is 0.8 and it should likely be lower. This is a simulation constraint and is done to ensure that the phenomenon is observable. In addition, the regeneration is started at a random time-step where there is visibly considerable deposition, instead of basing it on the spike in the pressure drop as in the case of DPFs. There is no sudden pressure drop increase in the case of a cylinder, as the domain does not get clogged like in the DPFs. The inlet concentration of soot, Y_{in}, is 1.6×10^{-4} (in terms of mass fraction). The contour plot shown in figure 5.1 is for consequent time-steps depicting together the evolution of temperature and the oxidation of soot.

It can be clearly seen that the regeneration starts at the front (towards the inlet) and progresses to the back side (outlet) of the filter, eventually oxidizing all the deposited soot around the cylinder and only the profile of the cylinder is seen. This is in harmony with the general pattern of the flow of gases in the filter as well as the progression of the temperature field as will be observed further in this report.

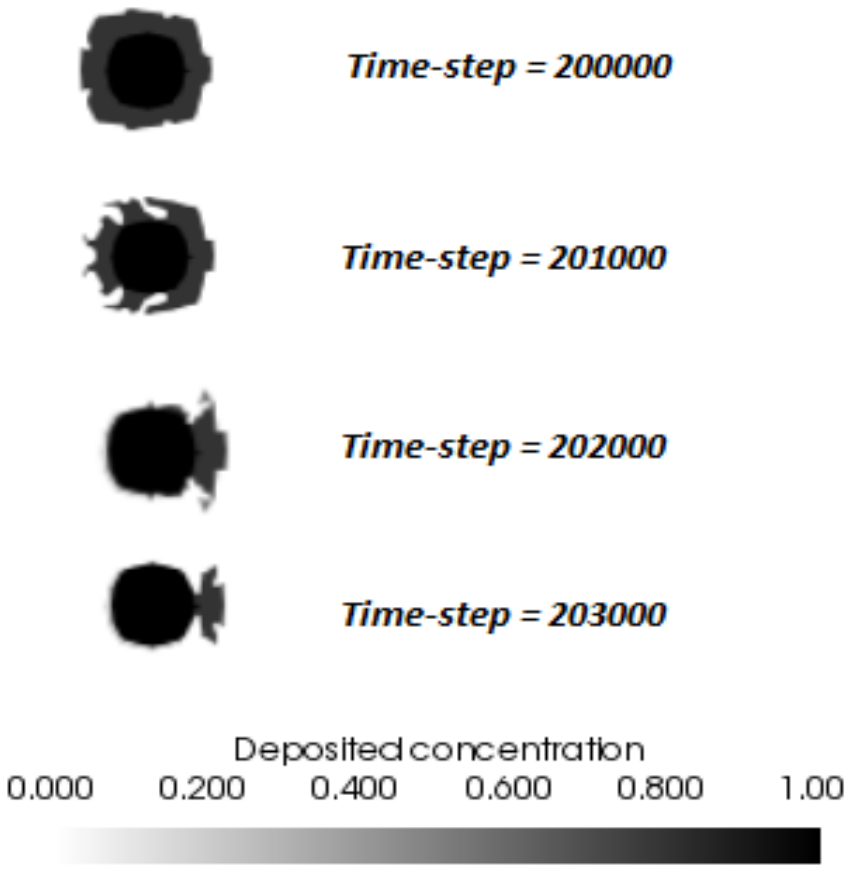

Figure 5.1 Flow over a cylinder: Regeneration at different time-steps, $P_s = 0.8$, $Y_{in} = 1.6 \times 10^{-4}$

In the next section, we discuss the implementation of the same regeneration model on the diesel particulate filters.

5.2 Regeneration in Diesel particulate filters

This section presents the results of regeneration phenomenon as observed in a Diesel particulate filter. As explained in earlier chapters of this report, the filter used for the simulation is a virtually generated two-dimensional porous media. This porous media is in line with a material called cordierite, which is a commonly used material for DPF substrates. By tuning the substrate sizes in the geometry of the porous media, other kind of substrates can easily be generated.

The Lattice Boltzmann method has a unit system of its own which is derived from the non-dimensional forms of the physical units. The correspondence between the three systems (Physical units, non-dimensional units and LB units) is made through dimensionless or scale independent numbers (Reynolds number, Prandtl number). The results presented in this section are in physical units for reasons of accessibility. The conversion of units from physical to LB and back is presented in the Appendix A.

Several cases were run by tweaking a different parameter, for example velocity or inlet temperature, on each run. The probability of sticking, P_s in the range of 0.0001 – 0.003 was shown to be achieving the most realistic patterns of deposition in previous works [1], and so this range has been used in all the simulation runs in the current work. An inlet soot concentration of 1.6×10^{-4} (by mass fraction) is used in all the simulations. The oxidation is assumed to be at lean conditions, with an excess of oxygen present. The contour plots presented in figure 5.2 are for a filter with porosity $\phi = 0.9,$ depicting the deposited soot concentration against time as regeneration progresses. The probability of sticking. P_s is 0.002 and inlet velocity of 0.005 in LB units which translates to 0.142 m/s. The inlet exhaust gas temperature used is 0.01 in LB units or 573 K (300^o C) in Physical units. This case is referred to as case 1 or the ‘baseline case’ here on after. Results with variations in parameters including pore size, inlet velocity and temperature as related to real world filters can be found by deciding on the simulation parameters in advance. This is discussed in detail in Appendix A.

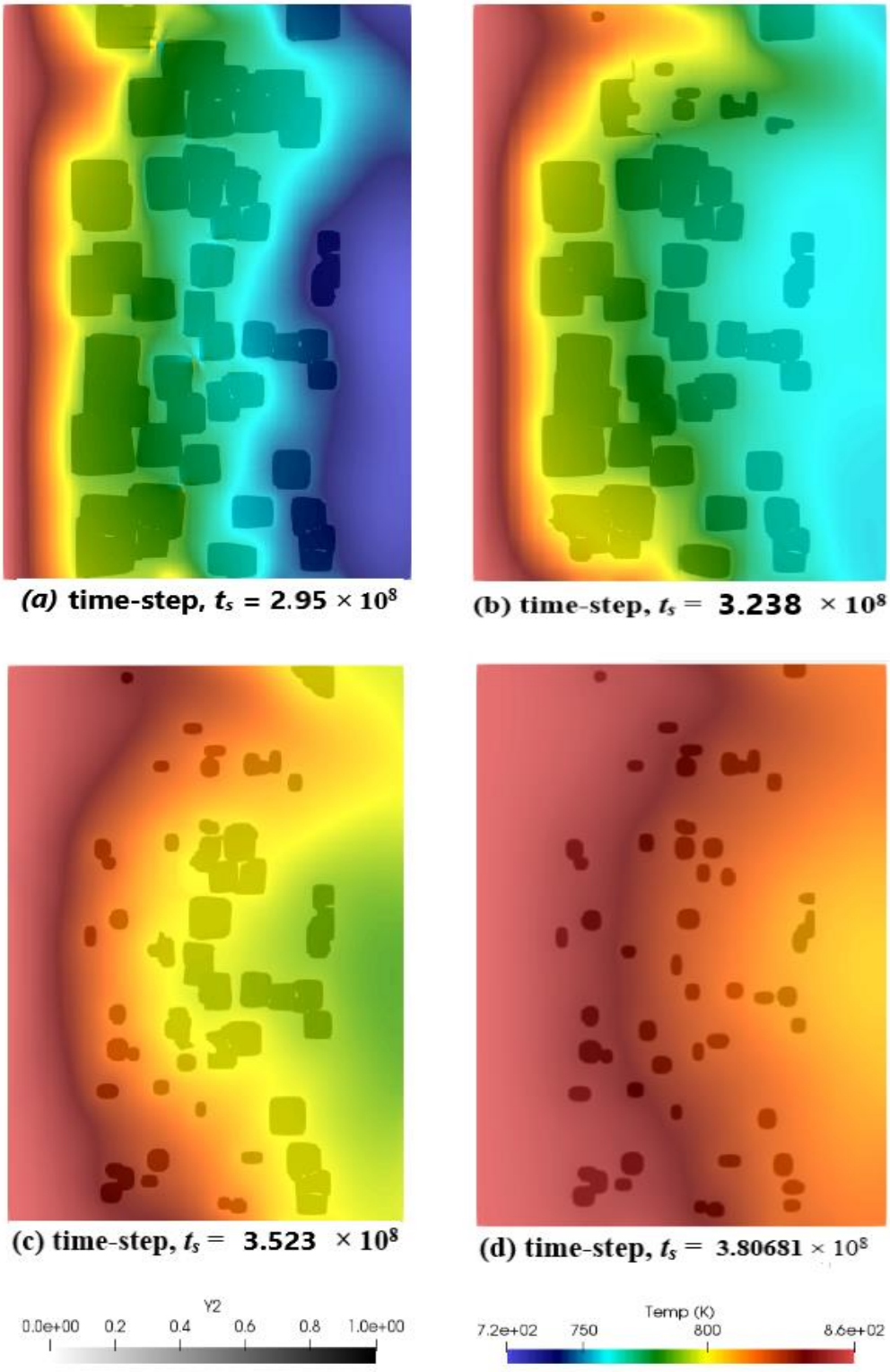

Figure 5.2 Regeneration of deposited soot concentration as seen with the progression of temperature field over time for case 1 (baseline case)

Figure 5.2 shows the evolution of temperature field with time and its effect on the deposited soot concentration. As mentioned in the previous chapter, the active regeneration of filters depends on a minimum threshold temperature below which the soot does not spontaneously oxidize. The threshold temperature used in all the simulations remains the same, 0.014 in LB units or 800 K in physical units. This temperature profile is represented by the orangish color in the figure 5.2. The deposited soot in this region and to the left of it (even higher temperature) starts vanishing gradually. The temperature solver raises the temperature slightly more than the threshold to make the process easily observable. Thus, the maximum filter temperature reaches the value of approximately 850 K, so a clear gradient in temperature is seen between the three temperature ranges (higher – threshold – lower) in the post-processed image. The 'time-steps' depicted in the figure correspond to seconds in real time and can be converted to physical units with the help of Reynold's number as depicted in appendix A. For ease of understanding, the plots presented from here on out are in physical units of time, temperature and pressure. The temperature gradient observed in the filter and the oxidation process occurring with it implies the successful reversal of the parametric probabilistic model. Also, this ascertains that i-LBM is effective in capturing not only the particulate matter accumulation physics, but also the physics of thermal diffusion and the chemical process of species oxidation.

Figure 5.3 shows the plot between peak filter temperature just before, during and after the regeneration process. The gradual rise in temperature is due to the inlet temperature elevation to the threshold value of 800 K, which is written into the code to simulate the injection of combustible substance which kicks off the regeneration process. It further increases to about 850 K due to reasons mentioned earlier. The temperature profiles can be seen to stay constant at this value during the time of regeneration, due to the heat of combustion, and then drop down gradually again once the regeneration has stopped. Although, it does not drop all the way down to the original value of 573 K. This is due to the conjugate heat transfer modeled into the code for the cordierite substrate of the DPF which retains the heat for a longer time.

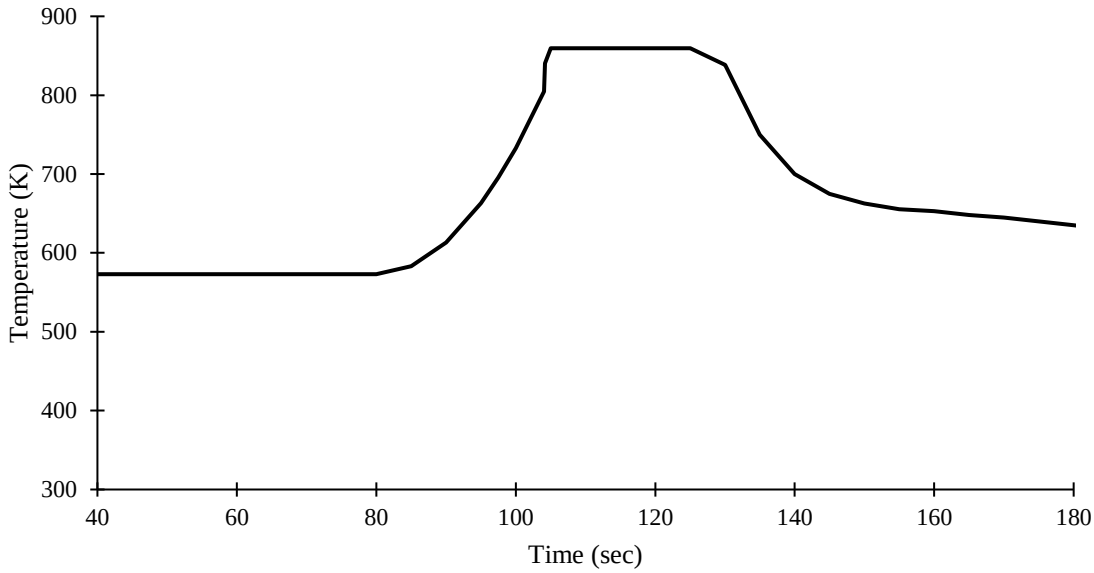

Figure 5.3 Plot of peak filter temperature (K) with time (sec), in the vicinity of the regeneration process

Further, figure 5.4 shows the plot of pressure drop across the filter against time. The pressure can be seen to drop gradually as the regeneration process starts from the left (cake layer) and sweeps through the entire filter with the progression of the temperature field. A close comparison of the pressure drop plot with the temperature plot reveals that the fall in pressure starts around the same point in time where the maximum temperature reaches threshold value. Similar trends of pressure drop during regeneration have been found by Kladopoulou et. al. [28].

Finally, figure 5.5 depicts the plot of deposited soot concentration inside the filter against time. The unit used for soot concentration is mass fraction. Again, it is seen that the soot retained inside the filter starts decreasing around the same time the temperature reaches threshold. The convex curve trend seen here is also similar to the experimental and simulation results obtained by researchers before [28, 22].

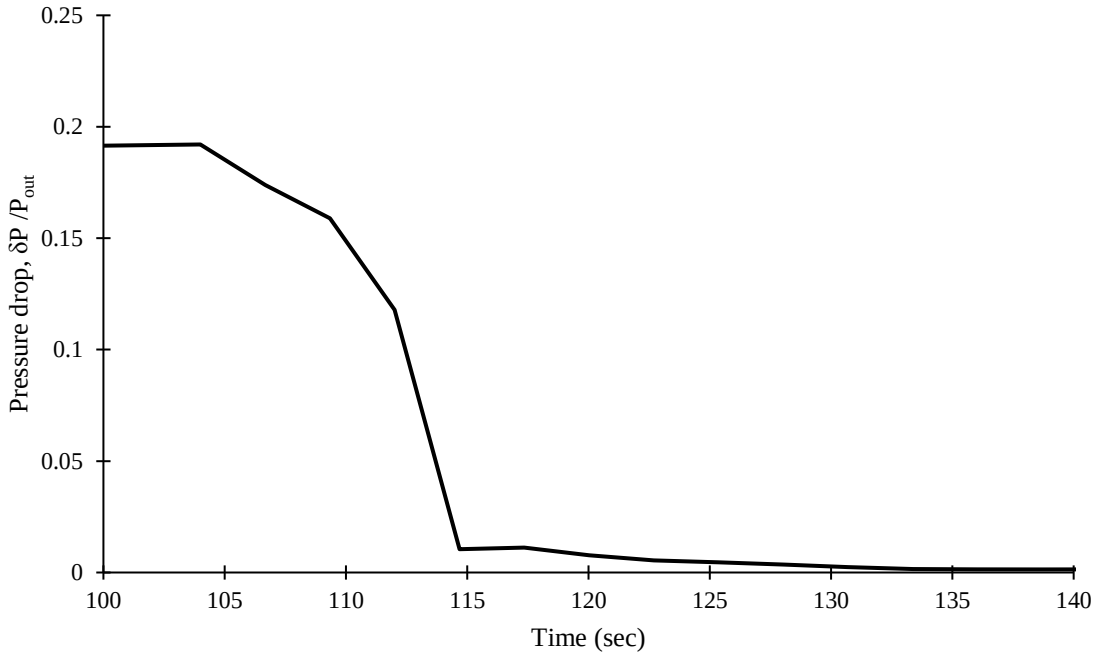

Figure 5.4 Plot of Pressure drop, $\delta p/P_{out}$ vs. time (in seconds) during regeneration in the filters

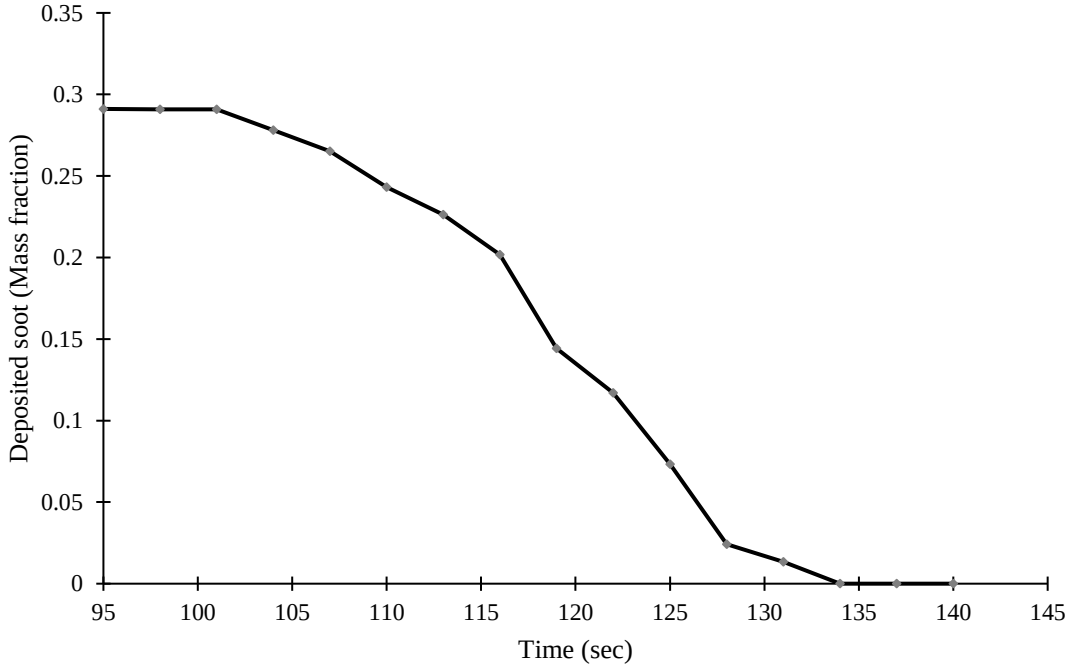

Figure 5.5 Plot of retained deposited soot concentration in the filter during regeneration

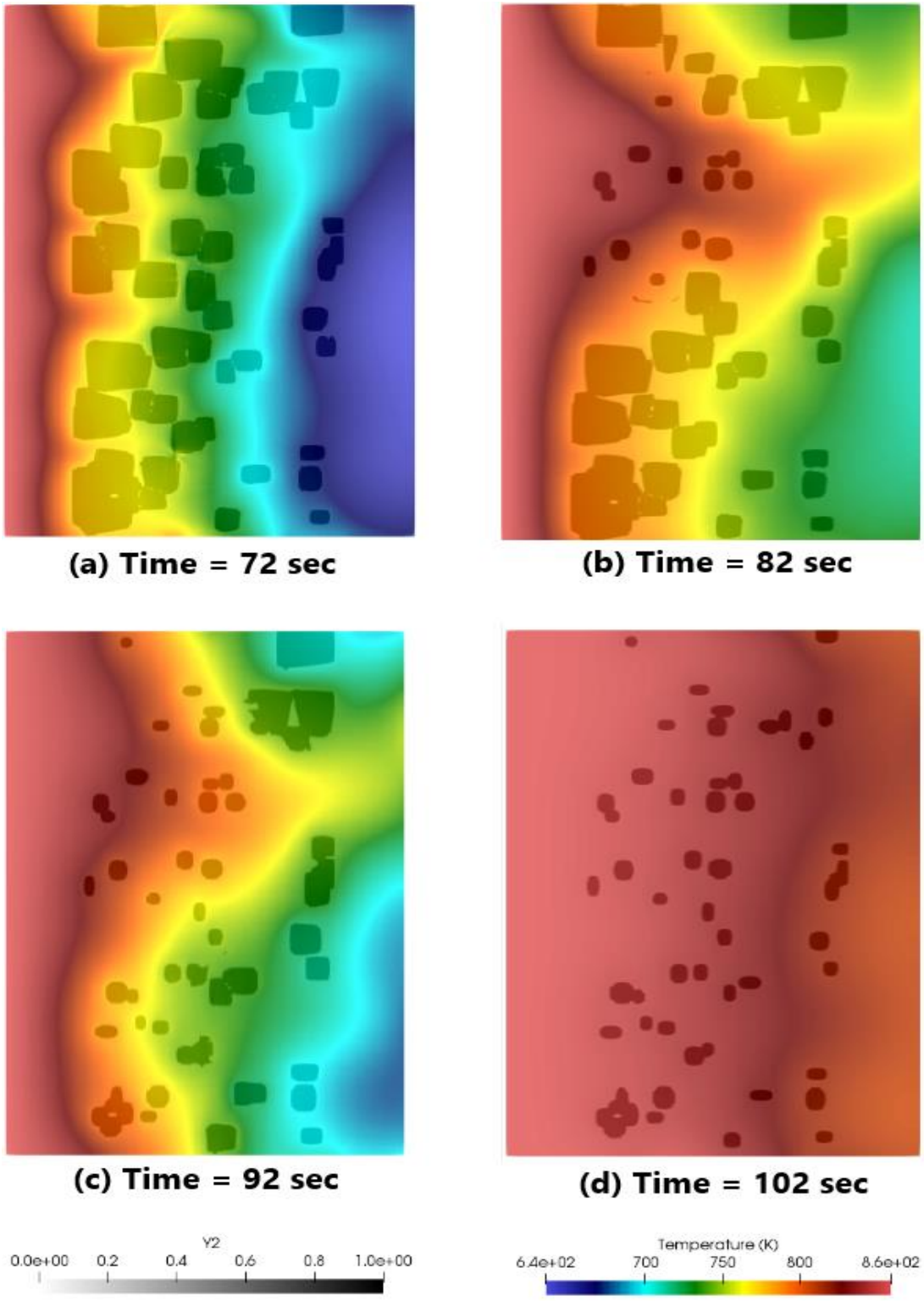

Figure 5.6 Regeneration of deposited soot concentration as seen with the progression of temperature field over time for case 2.

As mentioned earlier in this chapter, several cases were run of this simulation where in each run a certain input parameter was changed to demonstrate the behavior of the DPF at different physical conditions. The second of these cases involves increasing the inlet flow velocity to 0.008 from the previously used 0.005. This is a slight change in terms of physical units (0.142 m/s to 0.23 m/s), but prominent difference can be observed in the contour plots and the line graphs depicted. Figure 5.6 shows the contour plots for this case. It is clearly seen that due to the higher velocity, the temperature field blows through the middle of the filter in a skewed manner, leaving behind the cake layer towards the upper and lower walls untouched. This affects the pressure drop as is seen in figure 5.8.

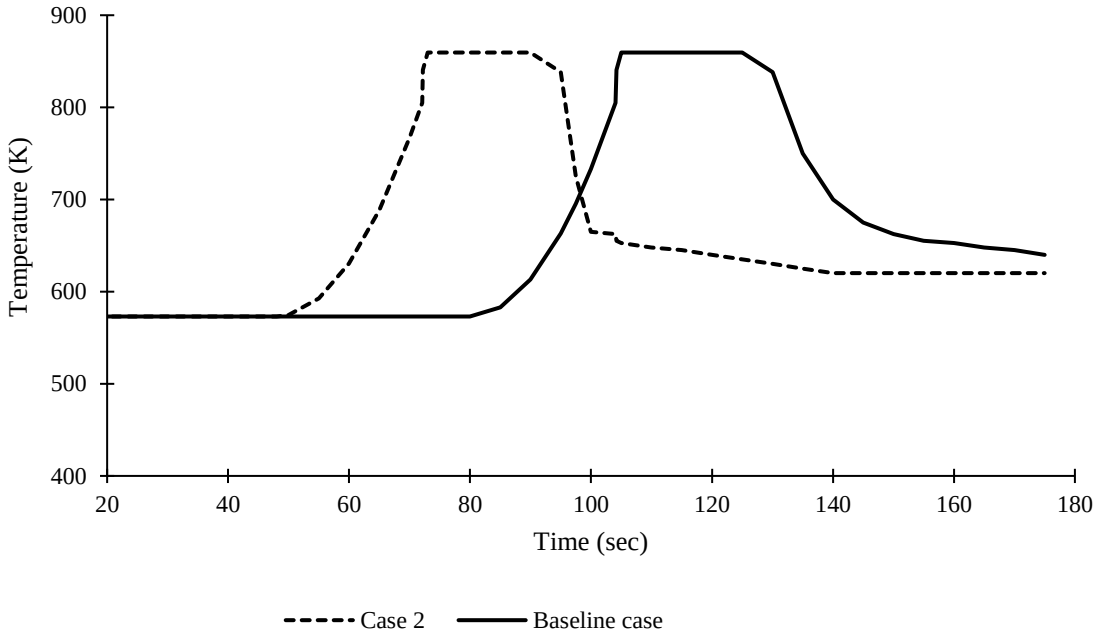

Figure 5.7 Comparison of peak filter temperature (K) vs. time (sec) for different values of inlet flow velocities

The gradual increase in the inlet temperature is dependent on pressure drop, as mention in the previous chapter. At a higher velocity the cake layer formation occurs faster than at lower velocity, and hence, the pressure drop increases faster in the higher velocity case.

This kick starts the process of inlet temperature rise, and thereby, regeneration occurs earlier. Also, once the regeneration process is over, the peak temperature curve drops in a steeper manner as the temperature field is washed out of the filter faster because of the higher velocity. The result is shown in figure 5.7. The plots of pressure drop and the retained soot concentration depict the same phenomenon, as shown in figures 5.8 and 5.9.

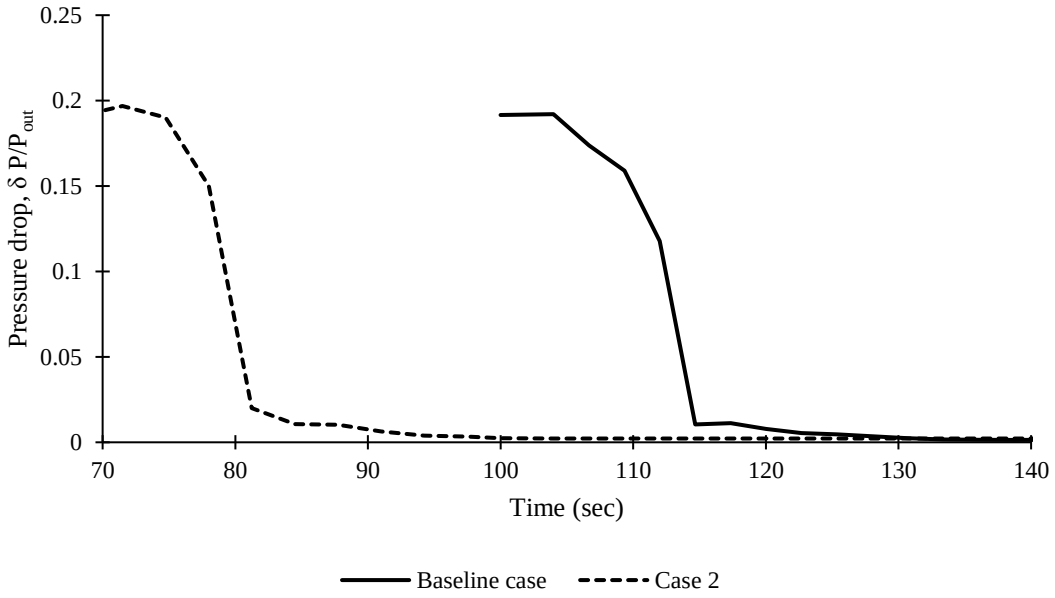

Figure 5.8 Comparison of Pressure drop, $\delta P/P_{out}$ vs. time (in seconds) for different values of inlet flow velocities

At higher velocity, the pressure drop curve is seen to be steeper than the one at lower velocity. As mentioned earlier, due to the high velocity the temperature field blows through the middle of the filter without touching the deposited concentration toward the outer cake layer. This action releases the back pressure instantly and the pressure drop curve thus drops down faster.

Now, soot cake layer is formed earlier in the higher velocity case than in the lower velocity case, which means that deposition of soot is skewed towards the front of the filter. The rate of deep bed filtration is lower in this case. Hence, the total amount of soot being filtered or deposited is less than that in the lower velocity case. In other words, the

filtration efficiency is low during higher velocity flow. This can be observed in the plot of retained soot concentration in figure 5.9. Also, it is observed that the oxidation process occurs faster in this case due to the temperature field's quick progression with higher velocity and hence, the retained soot concentration plot has a concave shape as opposed to the convex curve in the earlier case.

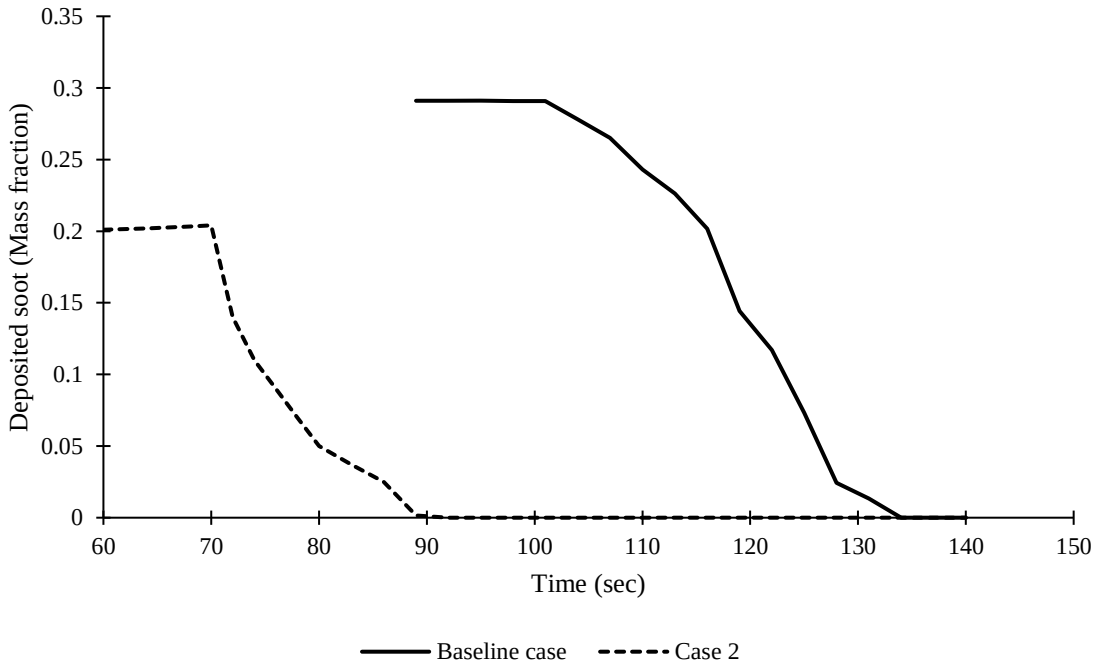

Figure 5.9 Comparison of deposited soot concentration (mass fraction) vs. time (sec) for different values of inlet flow velocities.

The next case under consideration involves increasing the inlet temperature to 1000 K, as opposed to the 800 K in the previous cases. This rise in inlet temperature is 200 K more than the threshold limit. The velocity and all the other input parameters are same as in the baseline case. The contour plot for this case is shown in figure 5.10 and the temperature profile in it progresses in an equivalent manner to that of the baseline case, with the only difference being that the temperature is higher in this case. The peak filter temperature, pressure drop and average retained soot concentration are depicted in figures 5.11, 5.12 and 5.13 respectively.

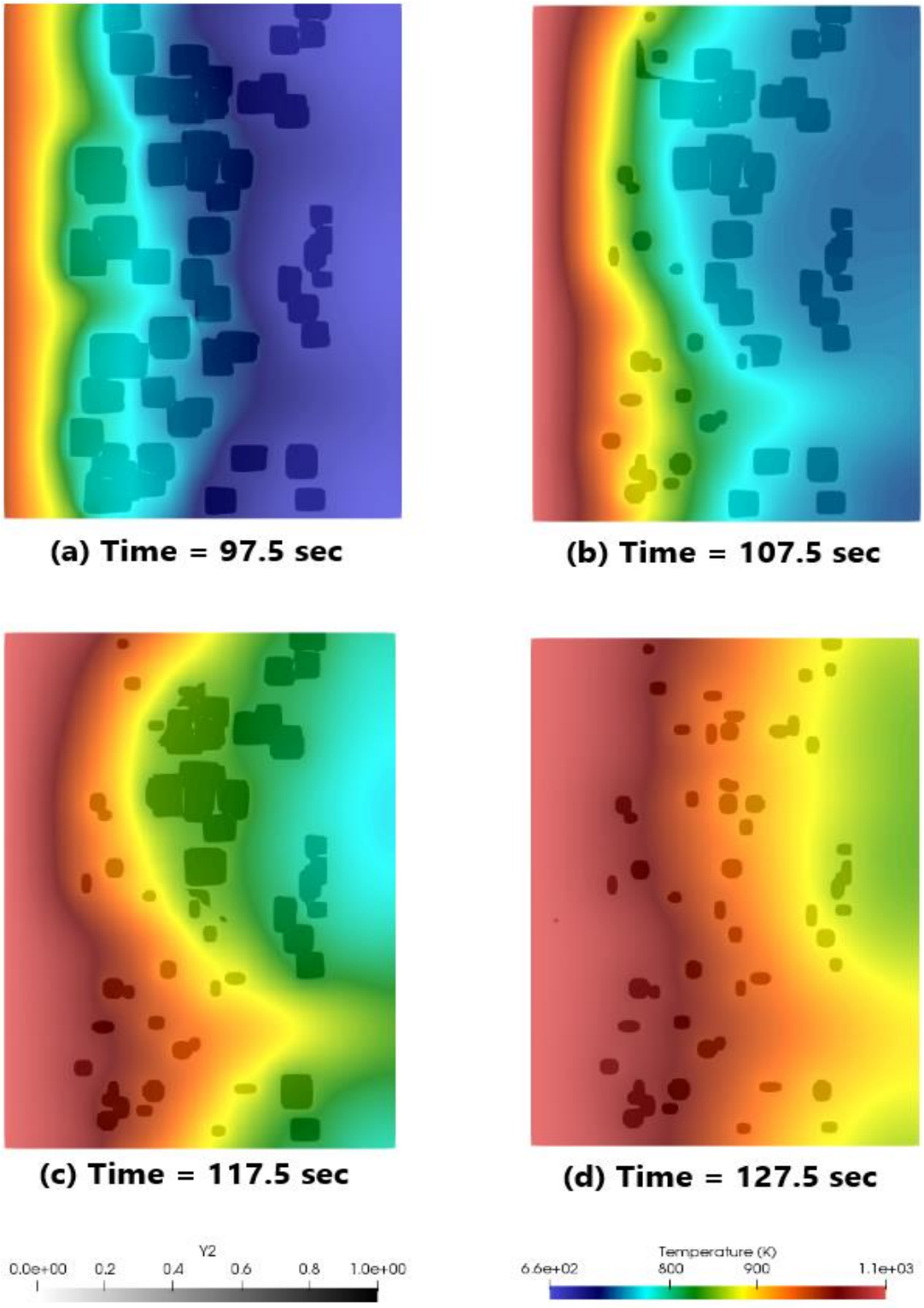

Figure 5.10 Regeneration of deposited soot concentration as seen with the progression of temperature field over time for case 3.

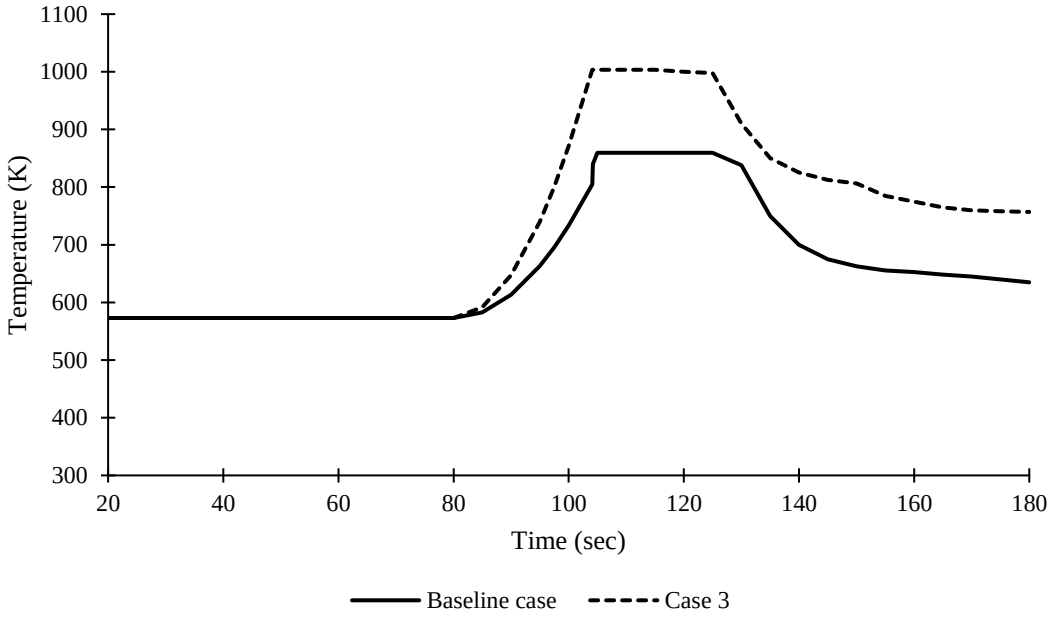

Figure 5.11 Comparison of Peak filter temperature (K) vs. Time (sec) for different values of inlet temperature increase

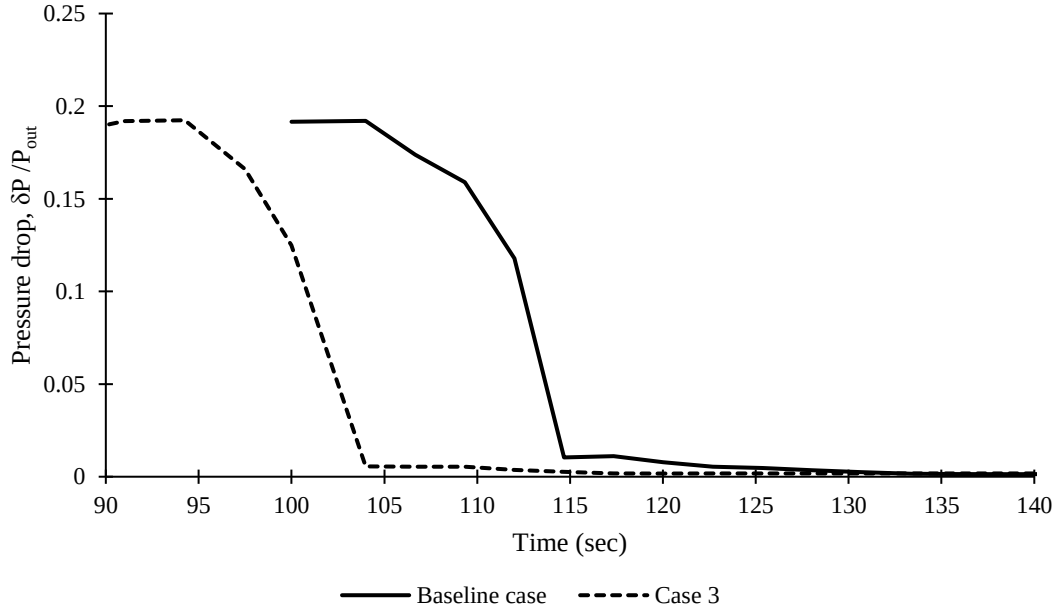

Figure 5.12 Comparison of Pressure drop, δP/Pout vs. time (in seconds) for different values of inlet temperature increase

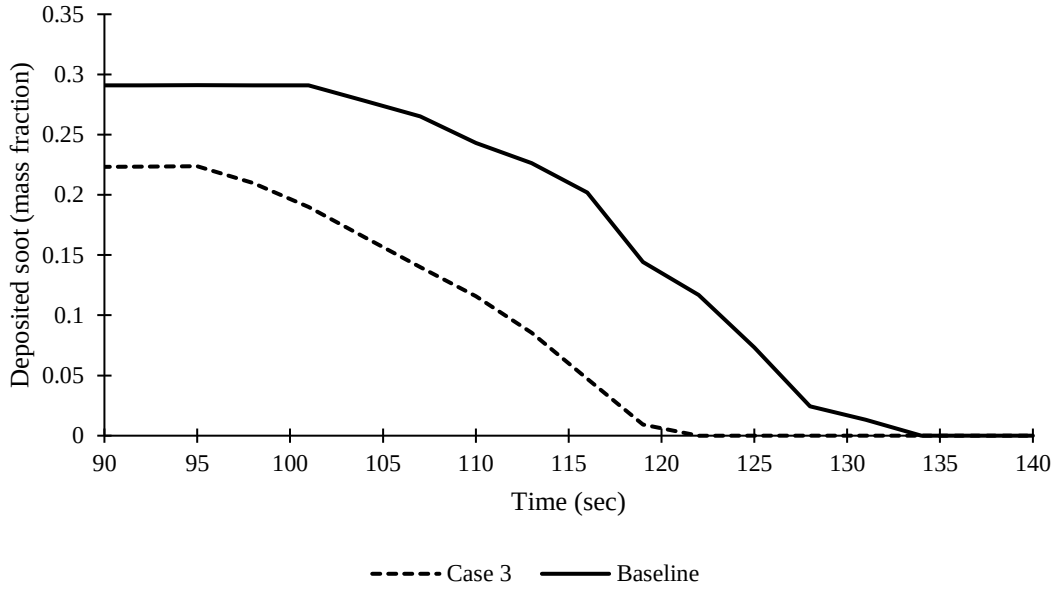

Figure 5.13 Comparison of deposited soot concentration (mass fraction) vs. time (sec) for different values of inlet temperature increase

The peak filter temperature comparison shows the inlet temperature rise in case 3 from 573 K to 1000 K and beyond. Since, in this case the threshold temperature is achieved slightly earlier than in the baseline case, there is comparatively lower amount of deposited concentration of soot in this case, which can be observed in figure 5.13. And the regeneration process ends earlier too. The trend of the pressure drop curve is only slightly different than that in the baseline case as it takes almost the same amount of time for the entire regeneration process in both case. The only difference is that regeneration occurs earlier than the baseline case.

The next and final case is that of a change in porosity of the filters. The porous media generator explained in the previous chapter is designed to create filters with different values of porosity and case 4 in this report uses a porosity of 0.7 as opposed to the 0.9 in the baseline case. Figure 5.14 through 5.17 depict the results for this case.

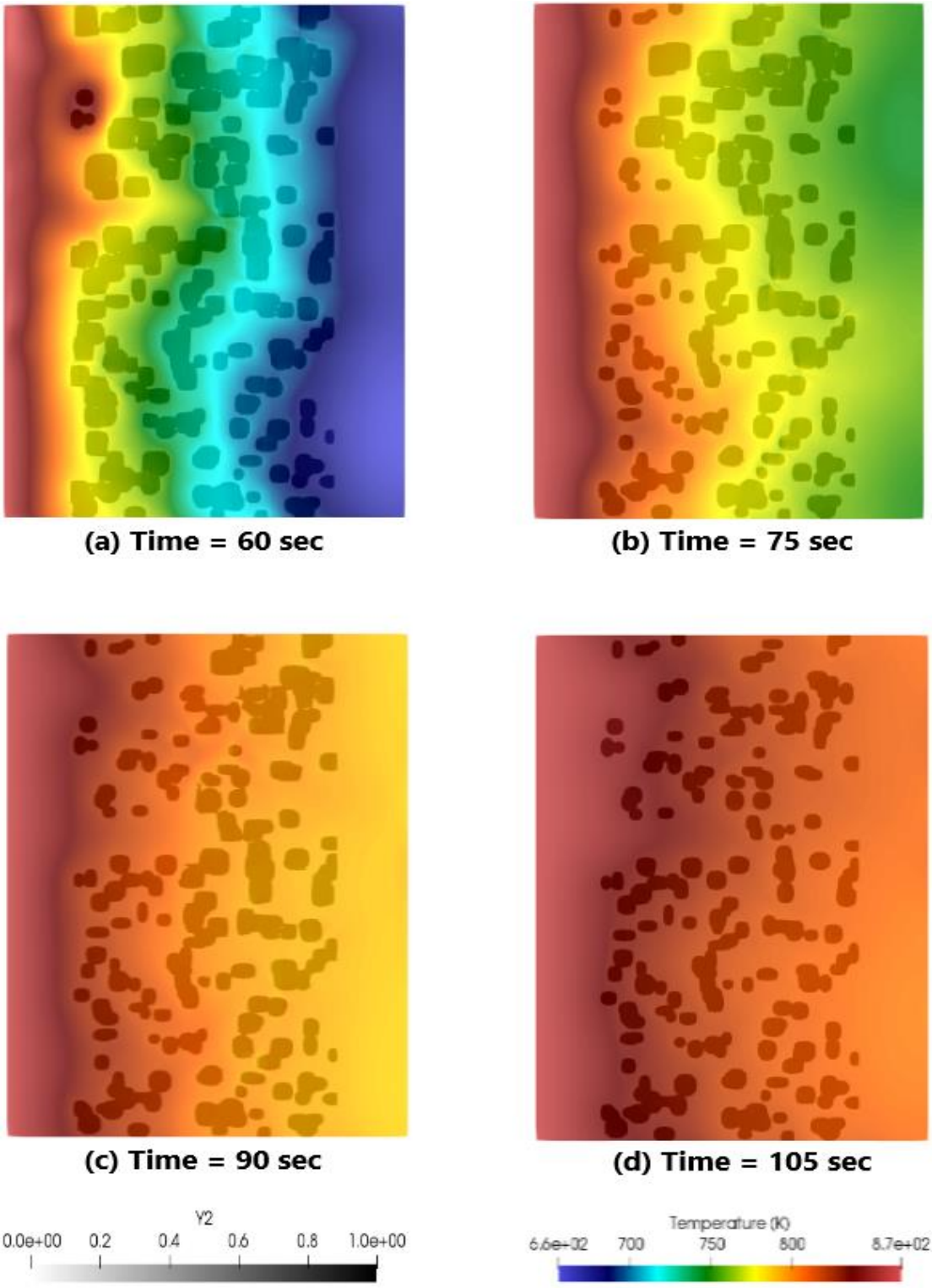

Figure 5.14 Regeneration of deposited soot concentration as seen with the progression of temperature field over time for case 4.

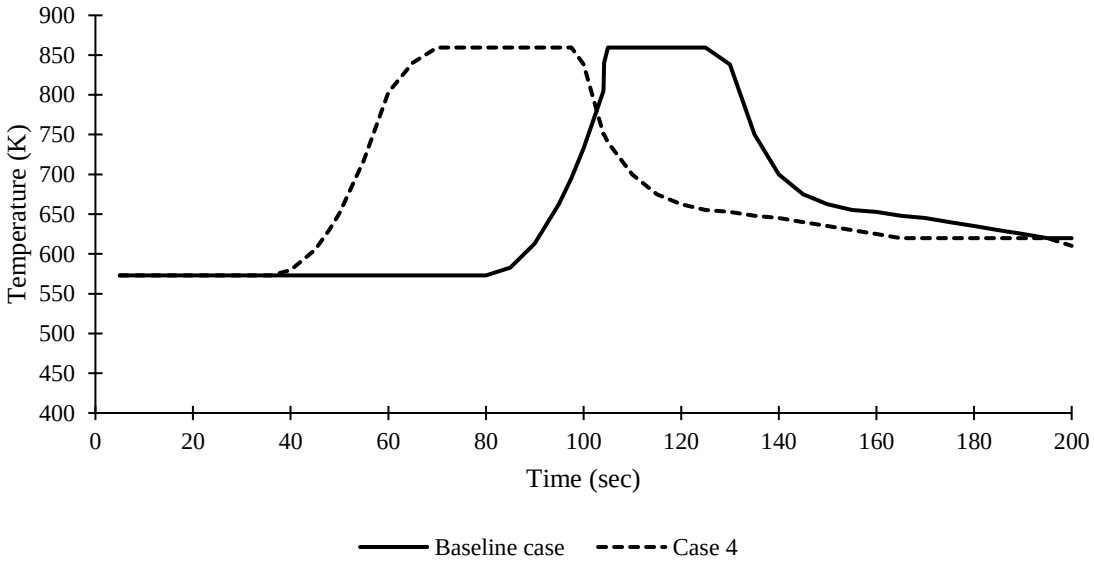

Figure 5.15 Comparison of Peak filter temperature (K) vs. Time (sec) for different values of porosity

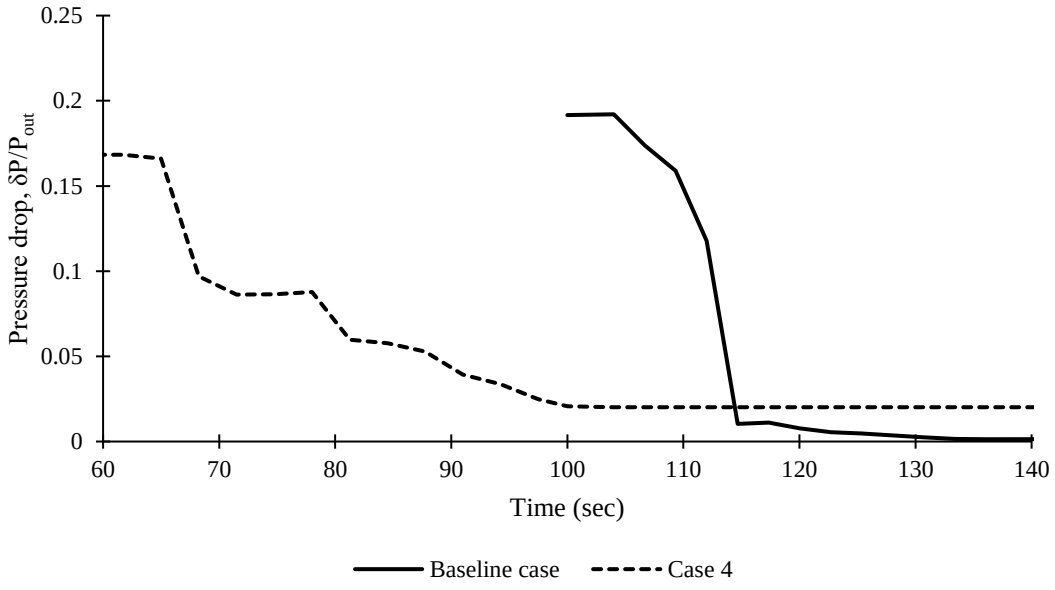

Figure 5.16 Comparison of Pressure drop, δP/Pout vs. time (in seconds) for different values of porosities

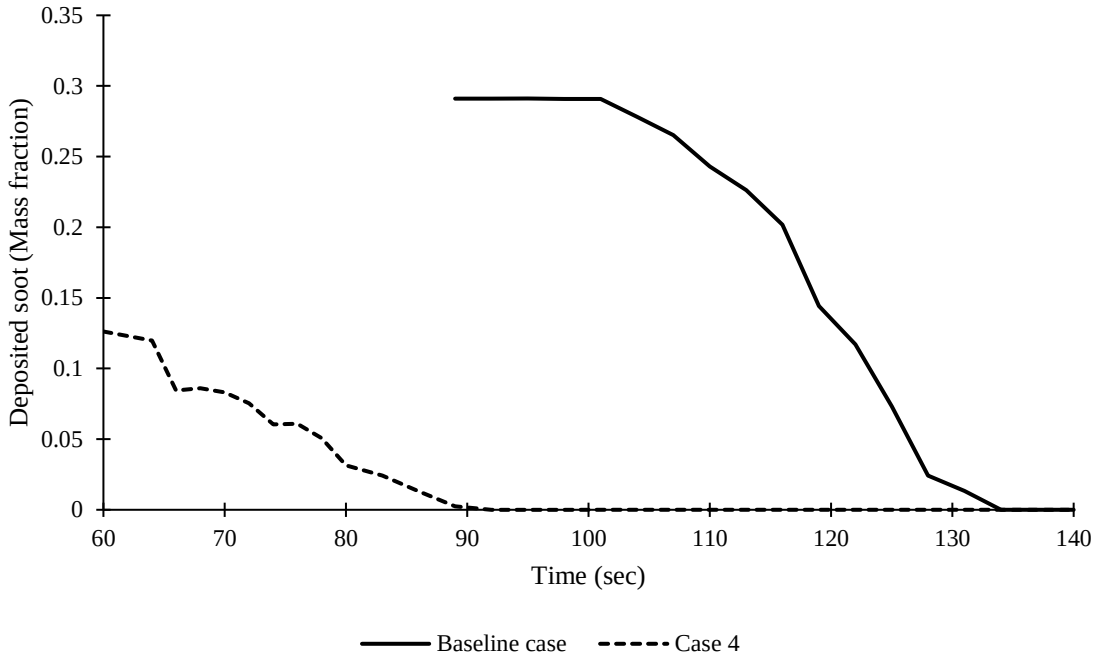

Figure 5.17 Comparison of deposited soot concentration (mass fraction) vs. time (sec) for different values of porosities

The comparison of peak filter temperature in the figure 5.15 shows clearly that the filter with lower porosity requires more time for the regeneration process to complete. This is because the flow has more obstructions in a low porosity filter which make the temperature field flow through the filter as well. And hence, it takes more time for the higher temperature to travel through the filter and complete the regeneration.

In figure 5.16, it is seen that the pressure drop curve is slightly chaotic with the pressure drop value going constant for small intervals of time and then dropping again. This can be attributed to the geometry of the low porosity filter, as seen in the contour plot (figure 5.14), which is more complex than the one with higher value of porosity. As mentioned earlier, this makes the flow through the filter more chaotic and slower as the flow tries to find new pathways to pass through. Meanwhile, the farther end of the filter where the temperature field has not yet reached keeps depositing soot onto the substrate. This increase in the deposited soot makes the porosity decrease even further which in turn is

the cause of pressure drop rise. But in this case, the rise in pressure drop due to deposition at the farther end is compensated by the regeneration process already going on at the front end. Thus, the pressure drop curve finds and approximate balance and remains constant for small intervals. Same pattern is seen in the plot for average deposited concentration retained during regeneration for case 4.

Also, clearly visible in the three plots of comparison between the baseline case and case 4 is the fact that the filter clogs up very early for case 4, in turn kick starting the regeneration process earlier than all the other cases. And since the filter clogs up very early due to the already low porosity of the filter, the amount of soot filtered during the time before regeneration starts is the lowest of all the cases discussed in this report.

6 Conclusions and Future recommendations

6.1 Conclusions

In this study, the regeneration phenomena within a diesel particulate filter was simulated using an original approach to incompressible Lattice Boltzmann. A computer based disordered substrate generator with the flexibility of being able to generate filters with varied porosities was used. Works of previous authors on the transport and deposition phenomena in a filter were extended to get a complete picture of the entire inner workings of a diesel particulate filter.

An original algorithm for the simulation of regeneration phenomenon was developed. The implementation of the regeneration algorithm was exhaustively explained. Several parametric studies were conducted showing that the i-LBM and the virtual substrate effectively capture not only the physics involved in the soot accumulation phenomenon but also the physics of heat transfer and the chemistry involved in the soot oxidation phenomenon. The regeneration process was visualized as seen in experiments.

The results of the i-LBM simulation of the regeneration phenomenon were successfully plotted into corresponding physical values using the Reynold's and Prandtl number similarity considerations. It was inferred that an optimized set of LBM simulation parameters selected in priori is the best way to approach the process. Doing so provides more control over the real time to be simulated.

6.2 Future recommendations

Following are some points which possess a certain degree of scope of improvement on the current work:

1. The porous media generator used in the current work was designed in the 2-D space. This limits the functionality of the porous media generated for all porosities below 0.4 because of lower permeability. A 3-D substrate generator

needs to be created which facilitates the creation of a filter with appreciable permeability at lower porosities.

2. Creation of a 3-D porous media generator would also provide the ability to incorporate the conduction heat transfer effect within the membrane of the filter on which the cordierite substrate stands.
3. In the previous work related to the current work [1], and consequently, in the current work as well, the porosity of the soot-cake layer is not considered. This makes the pressure drop too sudden and affects the regeneration model which is initiated conditional to pressure drop fluctuation.
4. The regeneration model in the current work considers only active regeneration of the DPF. Models can be created to include passive regeneration or catalytic regeneration.
5. The chemistry, as related to the soot oxidation, has a scope of improvement. Various complex mechanisms for oxidation of process of soot can be considered, either from literature or experimentation and be modeled into the simulation by writing solvers for multiple species. The end results can thus be compared to experimental data more accurately.
6. The heat of reaction of soot needs to be accounted for, in greater detail.
7. The regeneration model is largely based on the reversal of the parametric probabilistic model used by researchers earlier. As a long-term goal, a mathematical model could be developed for regeneration.
8. The computation time can be greatly improved upon by using Distributed memory parallelism (Message passing interface, MPI) instead of the currently employed shared memory parallelism (OpenMP). This would greatly reduce the simulation run time on distributed systems.

7 References

[1] A. Ibrahim, "On Transport and Deposition phenomena in Diesel Particulate Filters using the Incompressible lattice Boltzmann method," Michigan Technological University, Houghton, Michigan, 2017.

[2] L. P. Kadanoff, "On two levels," *Phys. Today,* pp. 39:7-9, 1986.

[3] S. Chen and G. D. Doolen, "Lattice Boltzmann method for fluid flows," *Annu. Rev. Fluid Mech.,* pp. 30:329-364, 1998.

[4] J. Hardy, O. de Pazzis and Y. Pomeau, "Mlecular dynamics of a classical lattice gas: transport properties and time correlation functions," *Physical Review A,* p. 13(5): 1949., 1976.

[5] U. Frisch, B. Hasslacher and Y. Pomeau, "Lattice-gas automata for the Navier-Stokes equations," *Physical review letters,* p. 56(14): 1505., 1986.

[6] G. R. McNamara and G. Zanetti, "Use of the Boltzmann equation to simulate lattice-gas automata," *Physical review letters,* pp. 61(20), 2332, 1988.

[7] U. Frisch, "Lattice gas hydrodynamics in two and three dimensions," *Complex systems,* vol. 4, no. 1, pp. 649-707, 1987.

[8] F. J. Higuera and J. Jimenez, "Boltzmann approach to lattice gas simulations," *EPL (Europhysics Letters),* pp. 9(7), 663, 1989.

[9] P. L. Bhatnagar, E. P. Gross and M. Krook, "A model for collision processes in gases. I. Small amplitude processes in charged and neutral one-component systems.," *Physical review,* pp. 94(3), 511, 1954.

[10] *Personal communication with Mr. Aamir Ibrahim, Michigan Technological University.*

[11] A. A. Mohamad, Lattice Boltzmann method: fundamentals and engineering applications with computer codes, Springer science and business media, 2011.

[12] X. He and L. S. Luo, "Lattice Boltzmann model for the incompressible Navier–Stokes equation," *Journal of statistical Physics,* pp. 88(3), 927-944., 1997.

[13] Z. Guo, B. Shi and N. Wang, "Lattice BGK model for incompressible Navier–Stokes

equation," *Journal of Computational Physics,* pp. 165(1), 288-306., 2000.

[14] J. R. Murdock and S.-L. Yang, "Alternative and Explicit Derivation of the Lattice Boltzmann Equation for the Unsteady Incompressible Navier-Stokes Equation," *International Journal of Computational Engineering Research (IJCER),* pp. 6(12), 47-59, 2016.

[15] S. Succi, The lattice Boltzmann equation: for fluid dynamics and beyond, Oxford university press, 2001.

[16] M. C. Sukop and D. T. Thorne, Lattice Boltzmann modeling: an introduction for geoscientists and engineers., Springer Science and Business Media, 2007.

[17] Q. Zou and X. He, "On pressure and velocity boundary conditions for the lattice Bolzmann BGK model," *Phys. Fluids.,* vol. 9, no. 6, pp. 1591 - 1598, 1997.

[18] D. Fino and V. Specchia, "Open issues in oxidative catalysis for diesel particulate abatement," *Powder technology,* pp. 180(1), 64-73., 2008.

[19] J. C. Summers, S. Van Houtte and D. Psaras, "Simultaneous control of particulate and NOx emissions from diesel engines," *Applied Catalysis B: Environmental,* pp. 10(1-3), 139-156., 1996.

[20] A. G. Konstandopoulos, M. Kostoglou, E. Skaperdas, E. Papaioannou, D. Zarvalis and E. Kladopoulou, "Fundamental studies of diesel particulate filters: transient loading, regeneration and aging," *(No. 2000-01-1016). SAE Technical Paper.,* 2000.

[21] *Personal communication with Mr. John Murdock and Dr. Song-Lin Yang, Michigan Technological University.*.

[22] K. Yamamoto and S. Ohori, "Simulations on flow and soot deposition in diesel particulate filters," *International Journal of Engine Research,* vol. 14, no. 4, pp. 333-340, 2013.

[23] J. P. A. e. a. Neeft, "Kinetics of the oxidation of diesel soot," *Fuel,* vol. 76, no. 12, pp. 1129-1136, 1997.

[24] e. a. B. A. A. L. Van Setten, "Realistic contact for soot with an oxidation catalyst for laboratory studies," *Applied Catalysis B: Environmental,* vol. 28, no. 3, pp. 253-257, 2000.

[25] J. P. A. Neeft, *Ph. D. Thesis,* Delft, The Netherlands: Delft University of Technology, 1995.

[26] K. Leistner, "Experimental and Modelling Study of Catalytic Diesel Soot Oxidation," Paris, 2012.

[27] K. Yamamoto, X. He and G. D. Doolen, "Simulation of combustion field with lattice Boltzmann method," *Journal of statistical physics* , vol. 107, no. 1-2, pp. 367-383, 2002.

[28] E. A. Kladopoulou, J. H. Jhonson, S. L. Yang and G. G. Parker, "A Study Describing the Performance of Diesel Particulate Filters During Loading and Regeneration – A Lumped Parameter Model for Control Applications," SAE international, Houghton, MI, 2003.

[29] T. KrRuger, H. Kusumaatmaja, A. Kuzmin, O. Shardt, G. Silva and E. M. Viggen, "The Lattice Boltzmann Method," Springer, 2017.

[30] G. Stratakis, D. Psarianos and A. Stamatelos, "Experimental investigation of the pressure drop in porous ceramic diesel particulate filters," *Proceedings of the Institution of Mechanical Engineers, Part D: Journal of Automobile Engineering,* vol. 9, no. 216, pp. 773-784, 2002.

[31] K. Yamamoto and T. Sakai, "Simulation of continuously regenerating trap with catalyzed DPF," *Catalysis today,* vol. 242, pp. 357-362, 2015.

[32] K. Yamamoto, M. Nakamura, H. Yane and H. Yamashita, "Simulation on catalytic reaction in diesel particulate filter," *Catalysis today,* vol. 153, pp. 118-124, 2010.

[33] Y. H. Qian, D. d'Humières and P. Lallemand, "Lattice BGK models for Navier-Stokes equation," *EPL (Europhysics Letters),* pp. 17(6), 479., 1992.

[34] A. A. Mohamad and A. Kuzmin, "A critical evaluation of force term in lattice Boltzmann method, natural convection problem," *International Journal of Heat and Mass Transfer,* vol. 53, no. 2, pp. 990-996, 2010.

[35] Z. Guo, C. Zheng and B. Shi, "Discrete lattice effects on the force term in the lattice Boltzmann method," *Physical Review,* vol. 65, no. 4, p. 046308, 2002.

[36] L. S. Luo, "Theory of the lattice Boltzmann method: lattice Boltzmann models for nonideal gases," *Physical Reviews,* vol. 62, no. 4, pp. 4982-4996, 2000.

[37] N. S. Martys, X. Shan and H. Chen, "Evaluation of the external force term in the discrete Boltzmann equation," *Physical review,* vol. 58, no. 2, pp. 6855-6857, 1998.

[38] J. M. Buick and C. A. Greated, "Gravity in a lattive Boltzmann model," *Physical Review*, vol. 61, no. 5, pp. 5307-5320, 2000.

Appendix A

This appendix explains, in detail, the methodology followed to convert the Lattice Boltzmann based unit system used in this report to a physical system of units which is more comprehensible to the uninitiated. Section 2.8 presented a step-wise procedure to define simulation parameters by converting the pre-determined physical parameters into consistent LB units. The procedure in this appendix involves back-tracking the set of simulation parameters to a more explicit physical system of units. A simulation can thus, be setup without knowing the physical parameters and then using the law of similarities of the non-dimensional parameters the physical units can be derived [29].

Two non-dimensional parameters are to be considered as related to the physics problem presented in the current work – Reynold's number and Prandtl number. They represent the two-fold physics of the problem presented in the report – fluid transport and heat transfer.

Starting with the baseline case, we can use the simulation parameters presented in the table A-1. As a reminder, the baseline case was for a filter of porosity 0.9 at an inlet velocity 0.005 and probability of sticking 0.0005.

Using the Reynold's number similarity between the two systems of units (physical and LB) as explained in the section 2.8 of this report, we can write:

$$\tilde{\mathrm{Re}} = \frac{\tilde{u}\tilde{L}}{\tilde{\nu}} = \frac{uL}{\nu} = \mathrm{Re} \tag{60}$$

The above equation leads us to believe that if any three of the physical values are known and the physical system to which those values belong has the same Reynold's number, all the conversion factors can be calculated.

Table A-1 Simulation parameters

Physical Quantity	**LB units**
Inlet velocity, $\tilde{U}_{in}$	0.005
Density, $\tilde{\rho}$	1.0
Kinematic viscosity, $\tilde{\nu}$	0.167
Relaxation factor, $\tilde{\tau}$	1.0
Pressure, $\tilde{P}_{out}$	1.0
Reynold's number, $\tilde{Re}$	5.988
Inlet temperature, $\tilde{T}$	0.001
Thermal diffusivity, $\tilde{\alpha}$	0.25

The properties of air can be used for diesel exhaust gas calculation because the diesel exhaust contains Nitrogen (N_2) much like the ambient air. It can be thus said that the effect of any pollutant concentration in determining the physical properties of the diesel exhaust is confined to a minimal value [1]. Using the physical properties of air for diesel exhaust calculations, we get the value of kinematic viscosity and density to be $\nu = 4.7559 \times 10^{-5}\ m^2/s$ and $\rho = 0.6172\ kg/m^3$ respectively. The filter length is 600 μm [30] and its LB value is chosen to be 60 units. Using the values of the viscosity and filter length mentioned above and the values mentioned in the table A-1 we arrive at the physical value of inlet velocity, $U_{in} = 0.142\ m/s$. This value is within the limits mentioned in [22, 31, 32]. By changing the LB parameters as related to the other cases discussed in this report, we can find their respective physical results.

The conversion factors found as per the discussion above are:

$$\begin{aligned} &\textit{Density}, && C_\rho = 0.6172\ Kg/m^3 \\ &\textit{Velocity}, && C_u = \frac{U_{in}}{\tilde{U}_{in}} = 28.4\ m/s \\ &\textit{Viscosity}, && C_\nu = \frac{\nu}{\tilde{\nu}} = 2.8535\times10^{-4}\ m/s \\ &\textit{Length}, && C_L = \frac{L}{\tilde{L}} = 10^{-5}\ m \end{aligned} \tag{61}$$

Now, from the conversion factors found in (61) and using the simulation parameters presented in table A-1 we come to the conversion factors for time and pressure:

$$\begin{aligned} &\textit{Time}, && C_t = \frac{C_L}{C_u} = 0.0352\times10^{-5}\ s \\ &\textit{Pressure}, && C_P = \frac{C_\rho C_L^{\,2}}{C_t^{\,2}} = 621.55\ Pa \end{aligned} \tag{62}$$

Using the similarity of Prandtl number we can write:

$$\tilde{\mathrm{Pr}} = \frac{\nu}{\alpha} = \frac{\tilde{\nu}}{\tilde{\alpha}} = \mathrm{Pr} \tag{63}$$

From equation 63 we get the value of thermal diffusivity in physical terms as $\alpha = 7.1196\times10^{-5}\ m^2/s$ for air at temperature 573 K.

Next is the inlet temperature which is chosen to be 0.001 in the LB system. In real world applications, as explained in chapter 4 of the report, the inlet exhaust temperature is in the range of 550-600 K. The current work uses 573 K or 300º C. The conversion factor can thus be calculated as:

$$C_T = \frac{T}{\tilde{T}} = 57300\,K \tag{64}$$

The conversion factors are summarized in table A-2:

Table A-2 Unit conversion table

Physical Quantity	**Conversion factor**
Velocity, u	28.4 m/s
Density, ρ	0.6172 Kg/m^3
Kinematic Viscosity, v	2.8535×10^{-4} m^2/s
Length, L	10^{-5} m
Pressure, P	621.55 Pa
Temperature, T	57300 K
Time. t	3.52×10^{-7} s